Modelling the flow around and wake behind net panels using large eddy simulations

Gang Wang*[1], Tobias Martin[2], Liuyi Huang[1], and Hans Bihs[2]

[1]College of Fisheries, Ocean University of China, 266003 Qingdao, China
[2]Department of Civil and Environmental Engineering, Norwegian University of Science and Technology (NTNU), 7491 Trondheim, Norway

Ocean Engineering, 2021, **239** , pp. 109846.
DOI: http://dx.doi.org/10.1016/j.oceaneng.2021.109846

Abstract

The fluid flow through a fixed net panel is investigated using large eddy simulations. Computational meshing strategies suitable for smooth and fabric twines are proposed. Numerical validations are conducted by comparing with measurements of the flow around a circular cylinder and hydrodynamics of net panels. It is shown that the hydrodynamic simulation of a small portion of the net panel is sufficient to replicate the full-scale net. Hence, the effect of the incoming velocity, the diameter and the length of the twines on surrounding turbulence fields are studied. Unique flow patterns are revealed in contrast to existing side-by-side cylinder simulations. Distributions of turbulent kinetic energies in the wake region behind intersections are crucial. It is further shown that the net solidity has a more considerable impact on the flow patterns in the wake than the Reynolds number. Further, the velocity reduction through the net panel is determined by weighting the relative velocity over the net panel area in the far-field. The analysis reveals less velocity reduction in comparison to existing velocity reduction models based on theoretical derivations and good agreement with physical measurements. The comparison of smooth and fabric nets indicates additional shielding effects of the twisted configurations on the velocity reduction which is not addressed in previous studies.

Keywords: Turbulence; Flow fields; Wake; Net panel; Large eddy simulations

*Corresponding author, wg@stu.ouc.edu.cn
Postprint, published in Ocean Engineering, doi:http://dx.doi.org/10.1016/j.oceaneng.2021.109846

1 Introduction

In recent history, the tendency to move aquaculture farms to offshore regions arose to account for the increased demand for cultured fish and arising environmental concerns in coastal areas. The newly drafted concepts are typically large in size and require sophisticated approaches in the design phase. Offshore fish farms face extreme wave-current loadings from high-energy sea states resulting in increased fatigue and unpredictable structural damages Faltinsen and Shen (2018). In particular, the nets enclosing the biomass represent a sensitive part of the system suffering from the complicated environmental loadings, and eventual collisions with marine animals Zheng et al. (2019). An advanced understanding of the fluid flow through nets is required to quantify the hydrodynamics as well as the velocity reduction behind nets and, thereby, optimise future net designs.

The wake pattern behind nets has important practical implications on the structural responses of circular fish cages and the health of the enclosed fish. The presence of a large number of twine intersections induces complex flow patterns influencing the near-field around the net meshes Klebert et al. (2013) but also the wake region in the far-field Endresen et al. (2013). Measurements in the past were mainly concerned with mean properties such as loads and velocity reduction as dependencies of net solidity and inflow conditions. The turbulence properties of the fluid and wake patterns were however ignored mainly. This has severe implications for today's CFD models because they rely on experimental data to develop an approach to account for the influence of the net on the fluid. In order to improve the modelling capacity of existing RANS CFD models, it is therefore necessary to account for the correct replication of the flow patterns around and behind nets. The observation emphasises that the flow around net meshes cannot be predicted by assuming a superposition of the flow patterns around single cylinders Arne (2005). Osaka et al. (1983a,b) concluded from experiments that the resulting flow patterns are not a simple combination of two perpendicular wakes arising behind each cylinder. This also holds for the far-field of the wake.

Harendza et al. (2008) conducted PIV measurements to investigate the fluid velocity distributions around nets but did not present detailed studies of the turbulence structures. Cha et al. (2013) analysed the wake distributions behind copper nets based on PIV experiments. It was clarified that the flow characteristics depend particularly on the structural shape of the nets. A quantitative assessment of the turbulence behaviour in the wake region was not established, and no comparison to the more common fabric net material was conducted. More detailed fluid velocity distributions behind nets with varying solidity were obtained by Bi et al. (2013) using PIV and an acoustic Doppler velocimeter. It was shown that the solidity and angles of attack between fluid and net influence the velocity distribution in the wake downstream of the net. This conclusion was numerically confirmed in Endresen et al. (2013). Physical measurements inside and in the wake of a commercial salmon sea cage were performed by Klebert and Su (2020). It was indicated that aquaculture sea cages alter the magnitudes and distributions of the surrounding fluid velocities. Further, strong velocity reductions and high turbulence in the wake of cages, resulting in a notable effect on the circulations of micro-organisms in these regions, were reported. This emphasises the importance of turbulence for a successful design process of aquaculture cages in the future. In Lader et al. (2014), flume experiments were adopted to analyse the hydrodynamics of a cruciform structure representing a single mesh of the net. It was shown that the sphere in the cruciform configuration has a major influence on the forces and fluid distribution downstream. CFD simulations of the

time-averaged flow around a single cruciform were performed in Bi et al. (2017) and Tang et al. (2021) using a $k-\omega$ SST model and large eddy simulations, respectively. Here, velocity profiles around the cruciform were extracted, and the influences of the orientation, Reynolds number and blockage ratio on the fluid were analysed scientifically. Later, the time-averaged flow around and hydrodynamic drags on 2×2 net meshes were studied while varying the solidity in Wang et al. (2021). Further, a lattice Boltzmann model has been implemented and validated for the flow modelling around net planes in Tu et al. (2020). The study explored the dependency of the velocities downstream of the net for different angles of attack and solidity ratios. Nevertheless, the effects were not studied systematically for various inflow conditions and geometrical properties of the net. Thus, the unique flow patterns arising from the flow around multiple net meshes were not addressed in previous numerical studies. These patterns are however crucial for the accurate modelling of complete net panels. Also, the instantaneous flow and turbulence distributions around net panels, such as the dissipations of turbulent kinetic energies and intensities, are left to be studied. Here, a significant practical implication for the transport of particles in fish cages is expected.

It can be concluded that the existing experimental and numerical research lacks a detailed investigation of the fluid patterns, turbulence around and behind the nets. A systematic knowledge about the flow patterns around net panels is of significant importance because of its effect on the wake region behind nets. In particular, the twine material and weaving pattern, which relates to the material roughness, play an essential role in the expected hydrodynamics Tang et al. (2019). This study aims at adding knowledge by investigating the turbulent flow fields, including the time-averaged and instantaneous flows around net panels, and wakes using dynamic subgrid-scale large eddy simulations (LES) which model the effects of unresolved small-scale fluid motions within the filter, while the time and space dependence of the large-scale fluid motions are resolved. Two different materials, twisted 3-strand fabric and smooth copper, are utilized to perform a comparative study for the flow patterns around net meshes and in the wake. Here, the incoming velocity, as well as the diameter and length of the twines, are varied systematically. As the main result of the study, novel empirical formulae for the prediction of the velocity reductions behind a net panel are proposed on the basis of the CFD simulations, including the resolution of the turbulence in the fluid.

The structure of the article is as follows: Section 2 introduces the numerical model used in the study. This includes the description of the considered net panel (section 2.1), fluid dynamics solver (section 2.2) and computational setup (section 2.3). The accuracy of the numerical setup is accessed through a series of convergence and validation tests in section 3. The validated model is then applied to simulate the flow around net panels with various inflow conditions and net properties (section 4). The main foci are on investigating and quantifying the effect of the meshes on the mean fluid properties (section 4.1), the near-field turbulence properties (section 4.2) and the effects of the net on far-field velocity reduction (section 4.3). Conclusions arising from the presented studies are given in section 5.

2 Numerical model

2.1 Net panel

In this study, two kinds of classical square knotless nets are investigated numerically: Smooth copper nets (Fig. 1a,b and d, hereinafter abbreviated as SN) and 3-strand twisted fabric nets

(Fig. 1c and e, hereinafter abbreviated as TN). The twisted twine, which has the advantage of increased strength and simple processing, is the most widely utilised in fish farming Edwin et al.. The degree of twists has a crucial impact on the flow around each twine, especially for the vortex generation Jung and Yoon (2014). In the present study, a uniform degree of twisting of around 150 twists in 1m wire is chosen to model the fabric nets Sun (2009). Each net panel consists of multiple meshes arranged in a single plane, and each mesh is built from 4 individual twines. The geometrical properties of knotless square-mesh nets are typically reported in terms of the non-dimensional solidity ratio S_n and Reynolds number Re based on the thickness of the twines. They are defined as

$$\begin{aligned} S_n &= \frac{A_{\mathrm{pj}}}{A} = \frac{2dl - d^2}{l^2}, \\ Re &= \frac{U_0 d}{\nu}. \end{aligned} \tag{1}$$

Here, A_{pj} is the projected area of the net panel, A equals the area of the panel outline, while U_0, d and l refer to the undisturbed incoming velocity, diameter and length of each twine, respectively. Finally, ν denotes the kinematic viscosity of the fluid.

In the following sections, the flow patterns around nets perpendicular to the inflow are investigated under consideration of varying U_0, d and l. In order to cover a realistic range of the above parameters, 26 cases are simulated for SN and TN with U_0, d and l varying between 0.1 m/s and 1 m/s, $0.5 - 3$ mm and $0.01 - 0.03$ m. The influence of each factor on the flow field is studied while the other factors are remaining constant. The deformation of the net is neglected which is in accordance with the majority of hydrodynamics experiments investigating net panels with fixed corners Tsukrov et al. (2011); Zhou et al. (2015); Tang et al. (2017, 2019). A detailed overview of the cases is presented in Tab. 1.

Table 1: Overview of the cases used in the CFD study. SN stands for smooth twines and TN for twisted twines.

Case	U_0 **[m/s]**	d **[mm]**	l **[m]**	Re	S_n
SN1 / TN1	0.550	1.750	0.020	951.35	16.73%
SN2 / TN2	0.100	1.750	0.020	172.97	16.73%
SN3 / TN3	0.325	1.750	0.020	562.16	16.73%
SN4 / TN4	0.775	1.750	0.020	1340.5	16.73%
SN5 / TN5	1.000	1.750	0.020	1729.7	16.73%
SN6 / TN6	0.550	0.500	0.020	326.44	4.940%
SN7 / TN7	0.550	1.125	0.020	611.58	10.93%
SN8 / TN8	0.550	2.375	0.020	1291.1	22.34%
SN9 / TN9	0.550	3.000	0.020	1630.9	27.75%
SN10 / TN10	0.550	1.750	0.010	951.35	31.94%
SN11 / TN11	0.550	1.750	0.015	951.35	21.97%
SN12 / TN12	0.550	1.750	0.025	951.35	13.51%
SN13 / TN13	0.550	1.750	0.030	951.35	11.33%

2.2 Numerical fluid model

In a large eddy simulation (LES) a filtering operation which decomposes the velocity $U(x,t)$ into the filtered or resolved part $\overline{U}(x,t)$ and a residual component $u^{'}(x,t)$ is performed Pope

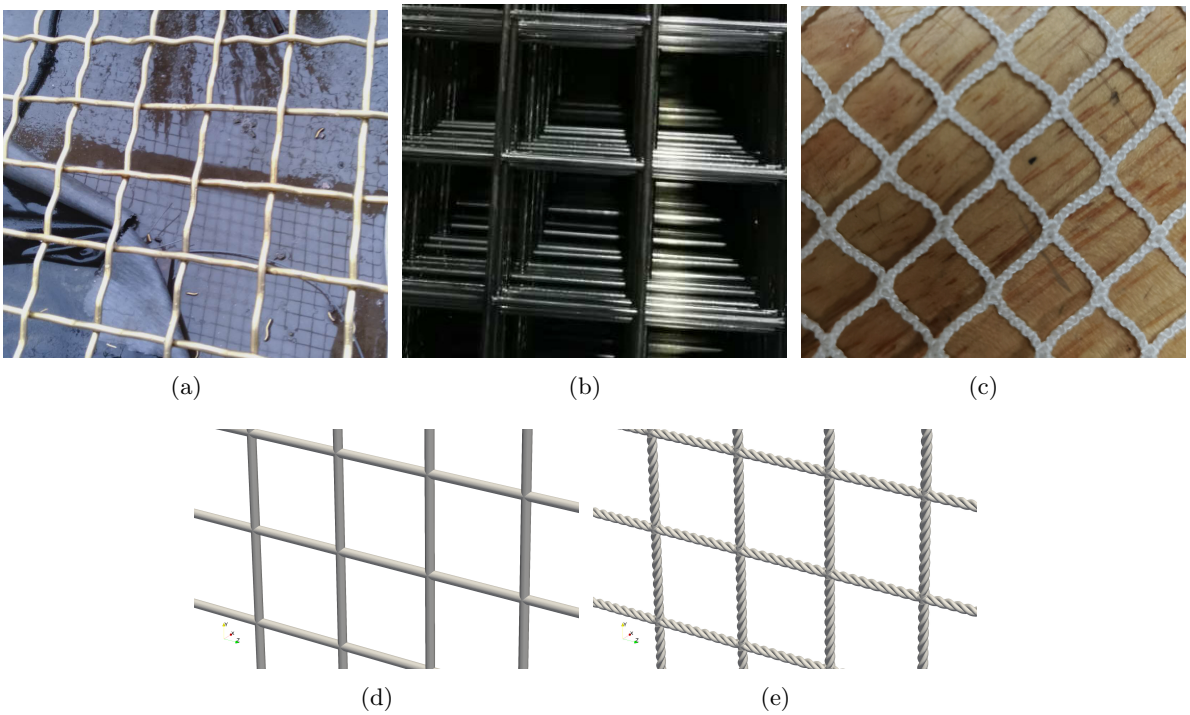

(a) (b) (c)

(d) (e)

Figure 1: Illustration of typical square-shaped net panels: (a) represents copper alloy braided nets; (b) corresponds to stainless steel welded nets; (c) is a twisted square fabric nets; (d) is the numerical smooth net SN1; (e) is the numerical twisted net TN1.

(2000). Then, the continuity and momentum equations of the filtered velocity fields $\overline{U}(x,t)$ for incompressible fluids are described in the conservative form as

$$\begin{aligned} \overline{\left(\frac{\partial U_i}{\partial x_i}\right)} &= 0, \\ \frac{\partial \overline{U}_j}{\partial t} + \frac{\partial \overline{U_i U_j}}{\partial x_i} &= -\frac{1}{\rho} - \frac{\partial \tau_{ij}^r}{\partial x_i} + \nu \frac{\partial^2 \overline{U}_j}{\partial x_i \partial x_j}, \end{aligned} \tag{2}$$

where ρ is the density, τ_{ij}^r denotes anisotropic residual stress tensor and ν represents the kinematic viscosity of the viscous fluid. The closure of the above equations is achieved through relating τ_{ij}^r and the subgrid-scale (SGS) stress tensor τ_{ij}^R Pope (2000), which is given as

$$\tau_{ij}^R = \overline{U_i U_j} - \overline{U}_i \overline{U}_j, \tag{3}$$

$$\tau_{ij}^r = \tau_{ij}^R - \frac{1}{3}\tau_{ii}^R \delta_{ij}. \tag{4}$$

Here, δ_{ij} is the Kronecker delta and τ_{ij}^r is modelled by a linear eddy-viscosity assumption of the SGS motion Smagorinsky (1963) as

$$\tau_{ij}^r = -2(C_S \overline{\Delta})^2 (2\overline{S}_{ij}\overline{S}_{ij})^{1/2} \overline{S}_{ij}, \tag{5}$$

with

$$\overline{S}_{ij} = \frac{1}{2}\left(\frac{\partial \overline{u}_i}{\partial x_j} + \frac{\partial \overline{u}_j}{\partial x_i}\right). \tag{6}$$

Here, C_S is the Smagorinsky coefficient and $\overline{\Delta}$ equals the length of the grid filter which is taking as the computational grid spacing in this simulation. Further, $\overline{S}_{ij}$ is the rate-of-strain tensor evaluated using the resolved velocity from the filter. A constant C_S can be adopted for fully-turbulent flows in the critical Re region Katopodes (2019) because the kinetic energies can be transferred unidirectionally from large-scale eddies to small scales where the dissipation occurs. However, C_S should be adjusted in near-wall regions or during different flow regimes, such as the laminar flow or the transition state to turbulence, to avoid deviated predictions of turbulent viscosity and massive dissipations Pope (2000). To overcome these drawbacks, a dynamic methodology for determining the local C_S proposed by Germano et al. (1991) and then improved in Lilly (1992) is adopted in the following investigations. Here, a test filter $\widetilde{\overline{\Delta}}$ with twice the width of $\overline{\Delta}$ is introduced and the residual stress based on the double-filtering process and the relevant deviatoric part are expressed as

$$\begin{aligned} T_{ij} &= \widetilde{\overline{U_i U_j}} - \widetilde{\overline{U}}_i \widetilde{\overline{U}}_j, \\ T_{ij}^d &= T_{ij} - \frac{1}{3} T_{kk}\delta_{ij} = -2C_S^2 \widetilde{\overline{\Delta}^2} (2\widetilde{\overline{S}_{ij}\overline{S}_{ij}})^{1/2} \widetilde{\overline{S}_{ij}}. \end{aligned} \tag{7}$$

which is related to Eq. (3) through the Germano's identity Germano et al. (1991):

$$\mathcal{L}_{ij} = T_{ij} - \widetilde{\tau_{ij}^R}. \tag{8}$$

Here, $\mathcal{L}_{ij}$ represents the resolved components of the turbulent stress and establishes the relation between the grid filter-based and test filter-based scales. The Smagorinsky model for the residual part of $\mathcal{L}_{ij}$ can be derived by subtracting the test-filtered τ_{ij}^r (Eq. (5)) from T_{ij}^d (Eq. (7)), which can be expressed as

$$\mathcal{L}_{ij}^r = T_{ij}^d - \widetilde{\tau_{ij}^r} = C_S^2 M_{ij}, \tag{9}$$

with

$$M_{ij} = 2\overline{\Delta}^2(2\overline{S}_{ij}\widetilde{\overline{S}_{ij}})^{1/2}\overline{S}_{ij} - 2\widetilde{\overline{\Delta}^2}(2\widetilde{\overline{S}_{ij}\overline{S}_{ij}})^{1/2}\widetilde{\overline{S}_{ij}}. \tag{10}$$

No single solution for C_S^2 can be obtained from Eq. (9) as it contains five independent subequations. To overcome this, the predicted errors of C_S^2 are minimised using a least squares method as described in Lilly (1992). Finally, C_S^2 is then calculated using

$$C_S^2 = \frac{\mathcal{L}_{ij}M_{ij}}{M_{ij}M_{ij}}. \tag{11}$$

All computations are conducted using the open-source CFD toolbox OpenFOAM. A transient solver with pressure-velocity decoupling based on the PISO algorithm (pisoFoam) is adopted. The temporal terms are discretised with the implicit second-order backward scheme, and diffusion terms are discretised using a second-order central difference scheme (CDS). The convective terms are discretised using a second-order linear upwind stabilised transport (LUST) scheme including 25% of fluxes obtained from a second-order upwind solution Warming and Beam (1976) into fluxes obtained with a CDS discretisation. This results in a low-diffusive method balancing accuracy and stability. A fixed time step related to the diameter of the cylindrical structures is set as $\Delta t = 0.002d/U_0$ so that the maximum Courant-Friedrichs-Lewy (CFL) number fluctuates between 0.12 and 0.2 for all simulations. The pressure equation is solved by the generalised geometric-algebraic multi-grid (GAMG) method, while the solver for the momentum and turbulence equations are based on a Gauss-Seidel algorithm with additional smoothing for improved convergence.

2.3 Computational domain and grid

As shown in Fig. 2, the computational domain of $al \times bl \times cl$ (length $\times$ height $\times$ width) is set in a Cartesian coordinate system with the origin located at the geometrical centre of the net panel. The net structure is central and coplanar in the global $y-z$ plane and 1/4 of the domain length in x-direction from the inflow. This configuration intends to eliminate the influences of the domain boundaries on the flow through the structure while ensuring a fully developed flow before reaching the net. The dimensions of the domain are based on the length of the twines. Subsequently, the coefficients a, b and c are fixed from the domain size convergence test performed in section 3.1.

A steady inflow with velocity U_0 and isotropic turbulence are initialised at the inlet located on the left side of the domain. The turbulent kinetic energy k and the specific dissipation rate ω are defined as

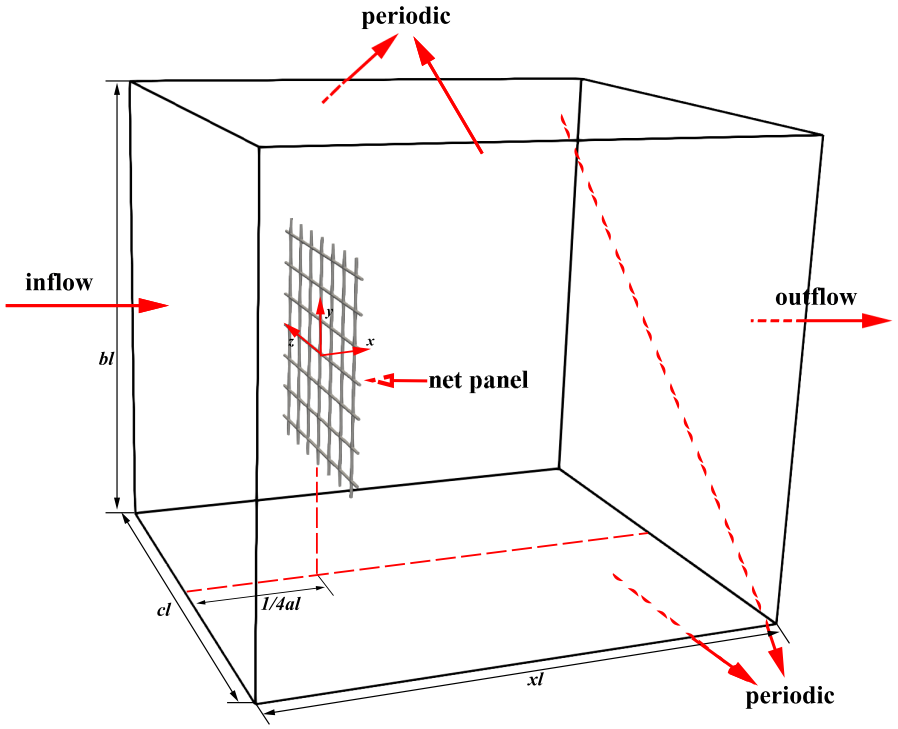

Figure 2: Computational domain and boundary conditions.

$$k = \frac{3}{2}(IU_0)^2,$$
$$\omega = \frac{k^{0.5}}{C_\mu^{0.25} L}, \tag{12}$$

with the turbulent intensity I which is estimated assuming a fully-developed turbulent pipe flow Adrian et al. (1994),

$$I = 0.16 R_{e_{d_h}}^{-1/8}, \tag{13}$$

with the $R_{e_{d_h}}$ using the pipe hydraulic diameter d_h. C_μ is a constant equal to 0.09, and L corresponds to the turbulent length scale calculated as given in Brørs (1999). Zero gradient Neumann conditions are set at the outlet for U, k and ω, and the pressure is set as zero. The side boundaries of the domain, as well as the top and bottom surfaces, are modelled as periodic boundary conditions. The fluid-solid interface is defined as a no-slip wall. For the cases including smooth material (SN), no wall function is applied at the net structure so that $y^+ < 1$ is ensured, i.e., the cell of the first layer near the structure is in the viscous sub-layer. In contrast, the complex geometry and roughness of fabric twines (TN) prevent a grid resolution of the sub-layer without significantly reducing the computational quality. Therefore, the wall function for modelling the surface roughness is used to model the sub-layer and roughness effects of the fabric material for the TN cases. It is based on the expression as

$$\nu_{t_w} = \max\Big(\min\Big(\nu_w \frac{y^+\kappa}{\ln(\max(E^{'}y^+, 1+10^{-4})-1}, 2\nu_{t,lim}\Big), 0.5\nu_{t,lim}\Big), \tag{14}$$

with

$$\begin{aligned} \nu_{t,lim} &= \max(\nu_{tw}, \nu_w), \\ E^{'} &= \begin{cases} E & K_s^+ \leq 2.25 \\ \dfrac{E}{f_n} & K_s^+ > 2.25 \end{cases}, \\ K_s^+ &= \frac{u^* K_s}{\nu_w}. \end{aligned} \tag{15}$$

Here, ν_w is the eddy viscosity of the fluid near the wall, ν_{tw} is the turbulent viscosity near the wall, κ represents the von Kármán constant, u^* is the friction velocity, E is the wall roughness parameter, f_n equals the roughness function coefficient, and K_s is the equivalent sand-grain roughness height. It is specified as 0.1 mm based on the surface roughness measurements of textile fabrics Vassiliadis and Provatidis (2004). Details about the other coefficients can be found in García et al. (2020).

The meshing tool SnappyHexMesh embedded in OpenFOAM is adopted to generate the grids around the net panel. The small diameter of the twines and the complexity of the numerous cruciform sub-structures require unstructured grids to ensure the preferable mesh quality Geremia and de Villiers (2012). An exemplary grid for the typical SN and TN cases are illustrated in Fig. 3. Three refinement zones are established to capture the turbulence fluctuations around the structures. The grid density in each refinement zone is twice as fine as the previous one. In the near-wall region, $13-15$ boundary layers with an expansion ratio of 1.13 are generated. The height of the first cell is calculated so that it is covered by the viscous sub-layer, i.e. $y^+ < 1$, for SN cases. For the fabric TNs, the first cell is located in the logarithmic layer to satisfy $y^+ > 11.63$. The velocity distribution near the surface is then modelled with the wall function of roughness.

2.4 Data analysis quantities

In the following sections, the time-averaged drag coefficient C_d is considered for quantifying the hydrodynamics around the different net configurations. It is calculated using the time-averaged drag force $\overline{F_d}$ and

$$C_d = \frac{2\overline{F_d}}{\rho A_{\mathrm{pj}} U_0^2}. \tag{16}$$

The pressure coefficient is calculated for the analysis of the flow around a cylinder using

$$C_p = \frac{\overline{P} - P_\infty}{\frac{1}{2}\rho U_0^2}, \tag{17}$$

with $\overline{P}$ the time-averaged pressure around the circumference of the cylinder and P_∞ the far-field static pressure. Further, the three-dimensional vortex motion is visualised using negative

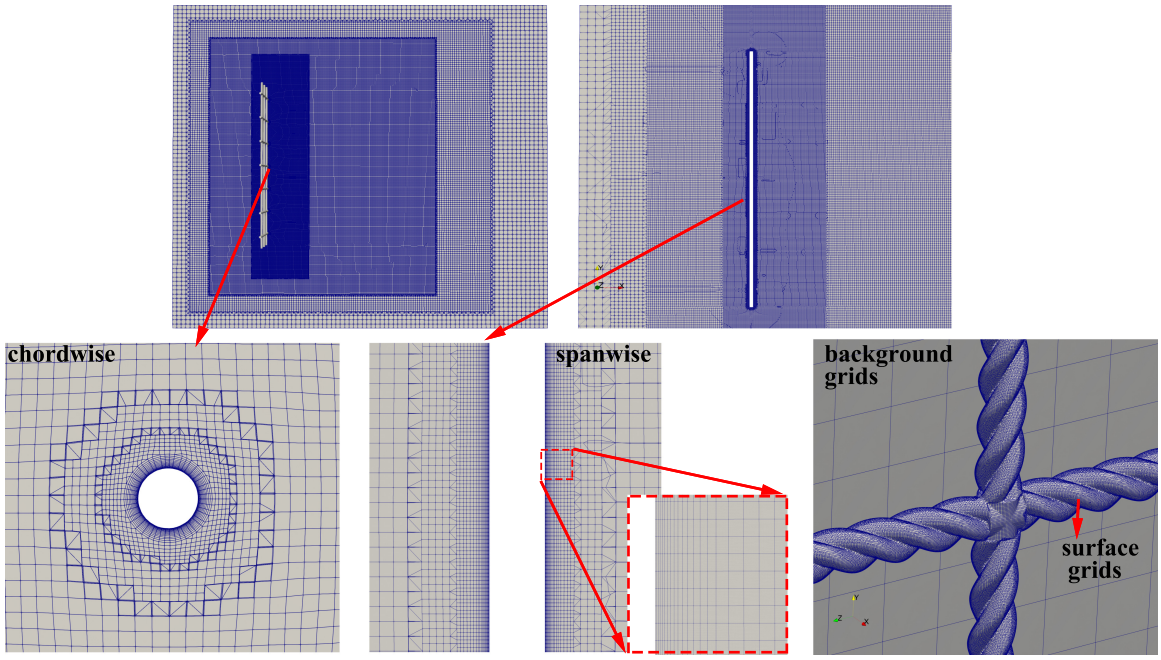

Figure 3: Computational grid and boundary layers around smooth and twisted twines (Case SN1 and TN1).

λ_2 values Zhou et al. (1999). They equal the second largest eigenvalue of the tensor A defined as

$$A = S_{ij}^2 + \Omega_{ij}^2. \tag{18}$$

Here, S_{ij}^2 and Ω_{ij}^2 are the strain rate tensor and rotation rate tensor, respectively. The intensity of the turbulence is analysed in terms of the total turbulent kinetic energy which is the sum of the modelled and resolved turbulent kinetic energy (TKE). The resolved part of the TKE is calculated using the root-mean-square (RMS) of the velocity fluctuations following the idea of isotropic turbulence.

3 Validation of the numerical model

3.1 Convergence studies

First, two convergence investigations related to the size of the domain and computational grid resolution are carried out. The domain size is chosen such that reflections from the side boundaries of the computational domain are not influencing the flow through the net. Later, this size is further adjusted to the outer dimensions of the investigated net panel, which varies with d and l. The grid resolution, including the non-dimensional grid density in the radial and span-wise directions Tang et al. (2021), is investigated such that the required accuracy is reached but the computations are as efficient as possible.

The convergence tests are carried out for the SN material with the parameters d = 2.05 mm, l = 25.4 mm and S_n = 0.155 which is taken from the *Welded-25* net (Fig. 5a)

in Tsukrov et al. (2011). The physical net has square knotless meshes and is made of Silicon-Bronze with a smooth surface. The panel has a size of 1 m × 1 m and is perpendicular to the flow direction. It is placed in a tank of 36.6 m × 3.66 m × 2.44 m at the University of New Hampshire. The incoming velocity is taken as 0.5 m/s corresponding to $Re = 1050$. A net panel portion consisting of 6×6 meshes, which is the largest dimension in the validation part below, is adopted to maximise the possible influence of the net meshes on the fluid. For the domain size analyses, the coarsest grid density (M1) is utilised to ensure no influence from under-resolved flow patterns in these studies. Tab. 2 provides an overview of the cases.

Table 2: Cases for the convergence studies of the domain size (D) and grid resolution (M). The inner region sizes denote grids of the innermost refinement zones. Δ/d represents the ratio between the first-layer grid cell size and the diameter of the bars, and Δ_z/d denotes the cylindrical span-wise density parameter.

Cases	**Domain sizes**	**Cases**	**Inner region sizes [m]**	**Maximum** y^+	Δ/d	Δ_z/d	**Cell number**
D1	$9.60l \times 8.00l \times 8.00l$	M1 (D3)	7.69×10^{-4}	0.88	8.29×10^{-3}	9.38×10^{-2}	15.2M
D2	$12.8l \times 11.2l \times 11.2l$	M2	6.67×10^{-4}	0.76	7.32×10^{-3}	8.13×10^{-2}	21.9M
D3	$16.0l \times 14.4l \times 14.4l$	M3	5.88×10^{-4}	0.67	6.34×10^{-3}	7.17×10^{-2}	28.6M
D4	$19.2l \times 17.6l \times 17.6l$	M4	5.21×10^{-4}	0.59	5.85×10^{-3}	6.35×10^{-2}	39.2M
		M5	4.72×10^{-4}	0.53	4.88×10^{-3}	5.75×10^{-2}	50.4M
		M6	4.17×10^{-4}	0.47	4.49×10^{-3}	5.08×10^{-2}	68.2M

Here, the distribution of C_p over the circumference of the middle point of net twines closest to side boundaries is extracted, which is presented in Fig. 4. The pressure coefficients of D1 indicate a significant boundary influence, whereas an increase of the domain size shows converged results. Considering the convergence and computational costs, D3 was chosen for the following grid independence study. In this case, the distance from the outer edges of the net panel to all side boundaries remains $3.7l$. Thus, the case M1 is the same as D3 in Tab. 2. The convergence of the simulated pressure distributions for increasing grid resolution is presented in Fig.4b. Differences are primarily observable for $\theta \leq 80°$, especially for the suction side behind the cylinder. Here, the coarsest grid M1 greatly overestimates the results due to the incapability of capturing the pressure fluctuation around the twine. For the cases M4-M6, the convergence of results is visible as the difference between the cases reduces. Therefore, the grid density in M5 with 49.3 million is considered for further studies. It can be noted that the non-dimensional densities of Δ/d and Δ_z/d in M5 are below 0.005 and 0.1, which are in accordance with previous LES of the flow around circular cylinders at comparable Reynolds numbers of $Re = 1000$ Lei et al. (2001); Zhao et al. (2009); Tang et al. (2021).

3.2 Validation of the hydrodynamic loads on net panels

The flow around each mesh of the net influences the surrounding meshes to some extent. As a result, it has to be ensured that the number of investigated meshes is chosen such that the influence from the surrounding net meshes is the same as for a full-scale net panel Wang et al. (2021). This step is further justified by the observation that the loads on a net panel are not the sum of the forces on multiple cross-shaped components, such as cylinders and spheres Balash et al. (2009). Considering the balance between computational cost and accuracy, it is necessary to investigate the effects of different numbers of meshes in the net

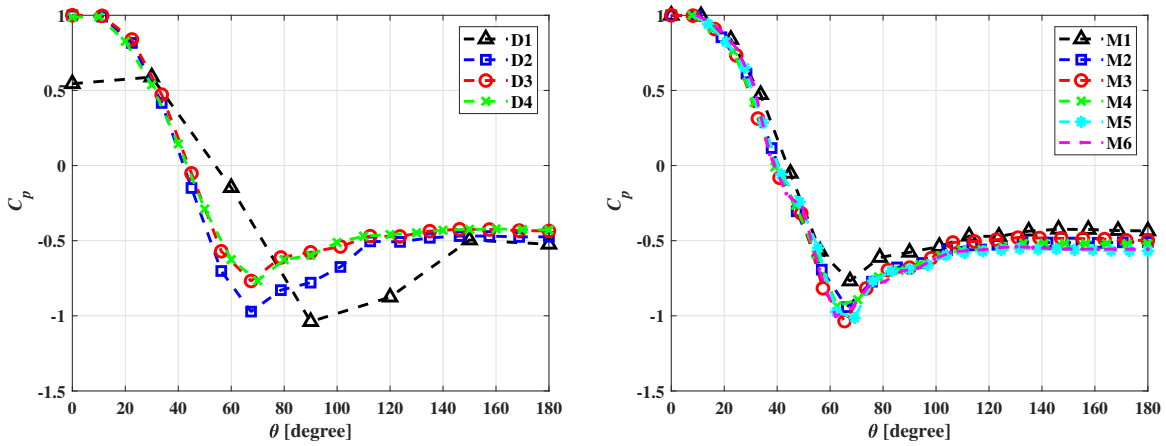

(a) (b)

Figure 4: C_p distribution around the circumference of the net twine close to the side boundary.

panel on hydrodynamics. In the following, this study is presented by comparing it to physical measurements. The considered dimensions are 3×3, 4×4, 5×5 and 6×6 meshes, and the obtained drag force coefficients as a function of Re are compared in Tab. 3.

The net model with a smooth material is compared to the experiments of the rigid net *Welded-25* in Tsukrov et al. (2011), of which normal drag force coefficients C_d are evaluated through a load cell. The relative deviation between numerical and experimental results is quantified using $\delta = (C_{d,num} - C_{d,exp})/C_{d,exp} \cdot 100\%$. Within a wide range of Re in Tab. 3, the increase of the mesh number reduces the difference between experiments and simulations. This suggests a stronger influence of the meshes with an increasing number of meshes. The largest relative deviation can be observed for Re around 900, which is still in an acceptable range because the average standard error of the force measurements is approximately $10-20\%$ Tsukrov et al. (2011). Consequently, 6×6 meshes are chosen for the following investigations.

For the twisted nets (TN), the validation is carried out based on the experiments of a full-size net panel with twisted 3-ply material Zhou et al. (2015) (Fig. 5b). Here, the hydrodynamic loads on a 0.7 m $\times$ 0.7 m nylon knotless net panel in a 9.0 m $\times$ 2.2 m $\times$ 1.95 m circulating flume tank were measured. The outer meshes were fastened tightly to a steel frame to prevent the deformation of the net. The panel was placed normal to the inflow with different constant velocities. The deviations to the experimental data are in a similar range as for the simulations of the smooth nets, with all errors below 10%. Furthermore, it is noticed that the drag forces of fabric nets are generally larger than that of smooth nets. This is mainly caused by the additional pressure forces induced by the twists and the frictional drag induced by the roughness.

3.3 Validation of the numerical model for the flow around a circular cylinder

As a final step, the numerical solver using LES is validated for the flow around a smooth circular cylinder at $Re = 320, 1000$ and 3900, in order to cover the investigated Re range

(a) (b)

Figure 5: Physical net models used for the investigation of a copper net *Welded-25* Tsukrov et al. (2011) and the twisted fabric net Zhou et al. (2015) in static current.

Table 3: Comparison of the drag force coefficient between experiments and CFD simulations for different number of meshes composing the net panel.

Cases	**Dimensions**	Re	S_n	$C_{d,num}$	$C_{d,exp}$	δ
Wedled-25 in Tsukrov et al. (2011)	3 × 3	921.1	15.5%	0.9018	1.0495	-14.1%
	4 × 4			0.9155		-12.8%
	5 × 5			0.9253		-11.8%
	6 × 6			0.9539		-9.11%
	3 × 3	1601.9	15.5%	0.9051	0.9660	-6.30%
	4 × 4			0.9085		-5.95%
	5 × 5			0.9143		-5.35%
	6 × 6			0.9376		-2.94%
	3 × 3	2300.2	15.5%	0.9023	0.9596	-5.97%
	4 × 4			0.9134		-4.81%
	5 × 5			0.9103		-5.14%
	6 × 6			0.9308		-3.00%
Twisted(3-ply) in Zhou et al. (2015)	6 × 6	589.6	5.0%	1.4597	1.5836	-7.82%
		959.0		1.1521	1.1802	-2.38%
		1559.7		1.0634	1.1088	-4.09%

in Tab. 1. The time-averaged flow properties are analysed for the complete range of Re, while the instantaneous turbulence is additionally studied at $Re = 3900$ by comparing with the published data. The computational domain is specified as 30 $d \times 20$ $d \times 4$ d. The grid resolution, boundary conditions and numerical schemes are taken from the setup which is also used for the net panel cases below. In order to check the validity of the LES, the resolved proportion of the total kinetic energy (TKE) close to the near-field is presented in Fig. 6. In the majority of the wake region, over 80% resolved TKE is observable. In the free shear layers, turbulence is modelled due to the instabilities in these regions.

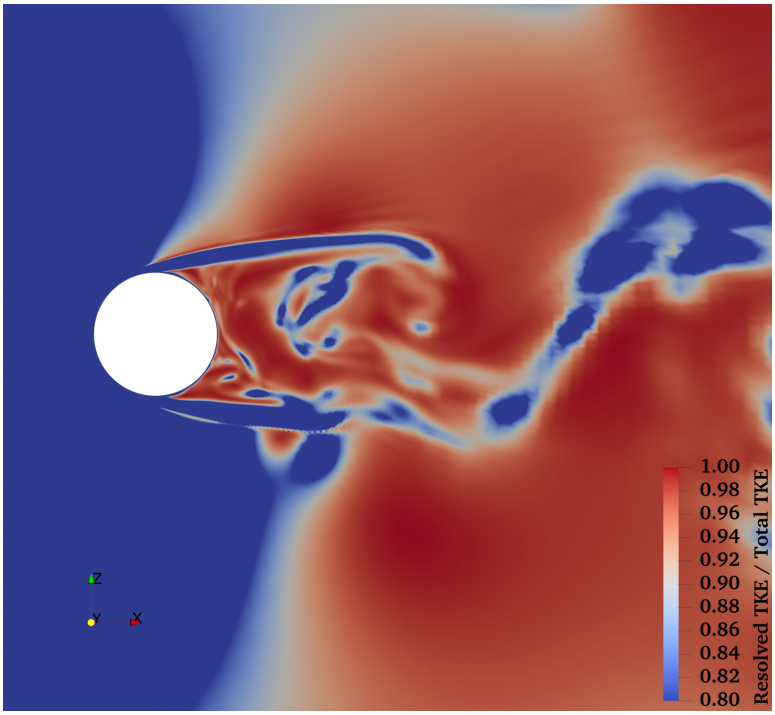

Figure 6: Profile of the proportion of the resolved turbulent kinetic energy for the flow around a circular cylinder at $Re = 3900$.

As a measure of the accuracy of the simulation, the wake behind the circular cylinder is analysed using the resolved mean Reynolds stresses and reported PIV experiments as well as LES simulations. Figs. 7a-d present the distribution of the resolved Reynolds stresses and stream-wise mean velocities at two different locations behind the cylinder. The chosen dynamic subgrid-scale model is capable of capturing the peaks and valleys at both $x/D = 1.06$ and 2.02, and the predicted results agree well with the published experimental and numerical data. Besides, the hydrodynamic pressure distribution around the circular cylinder at the critical $Re = 1.11 \times 10^5$ with a rough surface are modelled numerically and compared with the experimental measurement in Batham (1973). The roughness is achieved using a thin adhesive varnish and a uniform 0.5 mm-diameter sand layer, which can efficiently validate the roughness wall function used in this paper. It is illustrated in Fig. 7e that the fluctuation of C_p in the circumference direction is in accordance with the wind tunnel measurements. Additionally, the pressure fields around the circular cylinder at $Re = 320$, 1000 and 3900 are compared with the experimental data Norberg (2002); Cao et al. (2010); Norberg (1994) in

Fig. 7f, including the laminar and the transition to fully-turbulent states of the flow regimes. The numerical C_p for $Re = 1000$ and 3900 have been modelled accurately, while minor under-predictions of C_p are observed for θ>80° at $Re = 320$. It is attributed to the difference of the span-wise length compared with the experimental set-up, which has been already addressed in Norberg (1994); Tang et al. (2021).

4 Results and discussion

In the following, the simulations of the flow around net panels with smooth and fabric material properties are discussed. For detailed investigations, two representative cases (SN1 and TN1) are considered, whereas all cases from Tab. 1 are taken into account for general studies on the influence of the Re and net properties on the flow around the structure and in the near- and far-field wake. The setup is chosen from the convergence study presented above. The effects of multiple net meshes on the flow are discussed using the velocity and pressure fields close to the structure due to their importance for the correct determination of hydrodynamics effects on nets Bi et al. (2013). Here, the non-dimensional time-averaged velocity fields ($\overline{U}/U_0$) and the instantaneous vorticity profiles are analysed across two slices in two distinct directions. One slice is placed tangential (TP, Fig. 8c) and the other slices perpendicular (PP) to the net panel. Two perpendicular slices are considered: one is intersecting with the centre of the panel (PP1, Fig. 8a), and the other is perpendicular to the seven cross-sections of the twines (PP2, Fig. 8b). Thus, the difference of the flow characteristics behind the twines and the knots can be investigated as proposed in Cha et al. (2013). Finally, the flow patterns in terms of turbulence properties and velocity reduction are examined in the near- and the far-field wake behind the net panel. Based on these considerations, a novel formula for predicting the velocity reduction through nets is proposed.

4.1 Mean flow around the net meshes

At first, the mean velocity profiles are investigated. As illustrated in Fig. 9a-b, the predicted mean velocities are highly influenced by the twines and intersection locations for up to about one l behind the net. Here, the twisted structural characteristics show more influence on the affected region than the smooth nets, due to the rough twisted surfaces. The fluid separates behind each twine as expected and accelerates locally when passing the meshes which is consistent with the analyses in Bi et al. (2017). The results indicate that the boundary layer velocities for the smooth material are larger than for the twisted configuration which might be caused by the additional friction of these types of surfaces. At the same time, the length of the recirculation region behind the twines is larger for TN1 than for SN1. This coincides with previous observations in LES of smooth, wavy, and twisted cylinders Jung and Yoon (2014). It is further indicated in Fig. 9c-d that the flow is slightly blocked in front of the net panels. The degree of the blockage thereby varies between the central and outer meshes, and the complex surface of TNs leads to a higher blockage than for smooth material.

In the same figures, the so-called characteristic cross-flow velocity ($U_s = U/(1 - S_n)$) is marked in black around the twines. This velocity was assumed in Kristiansen and Faltinsen (2012) to approximate the velocity related forces on net panels while deriving their screen force model. The presented results confirm the validity of this assumption for these types of nets for the first time using CFD simulations.

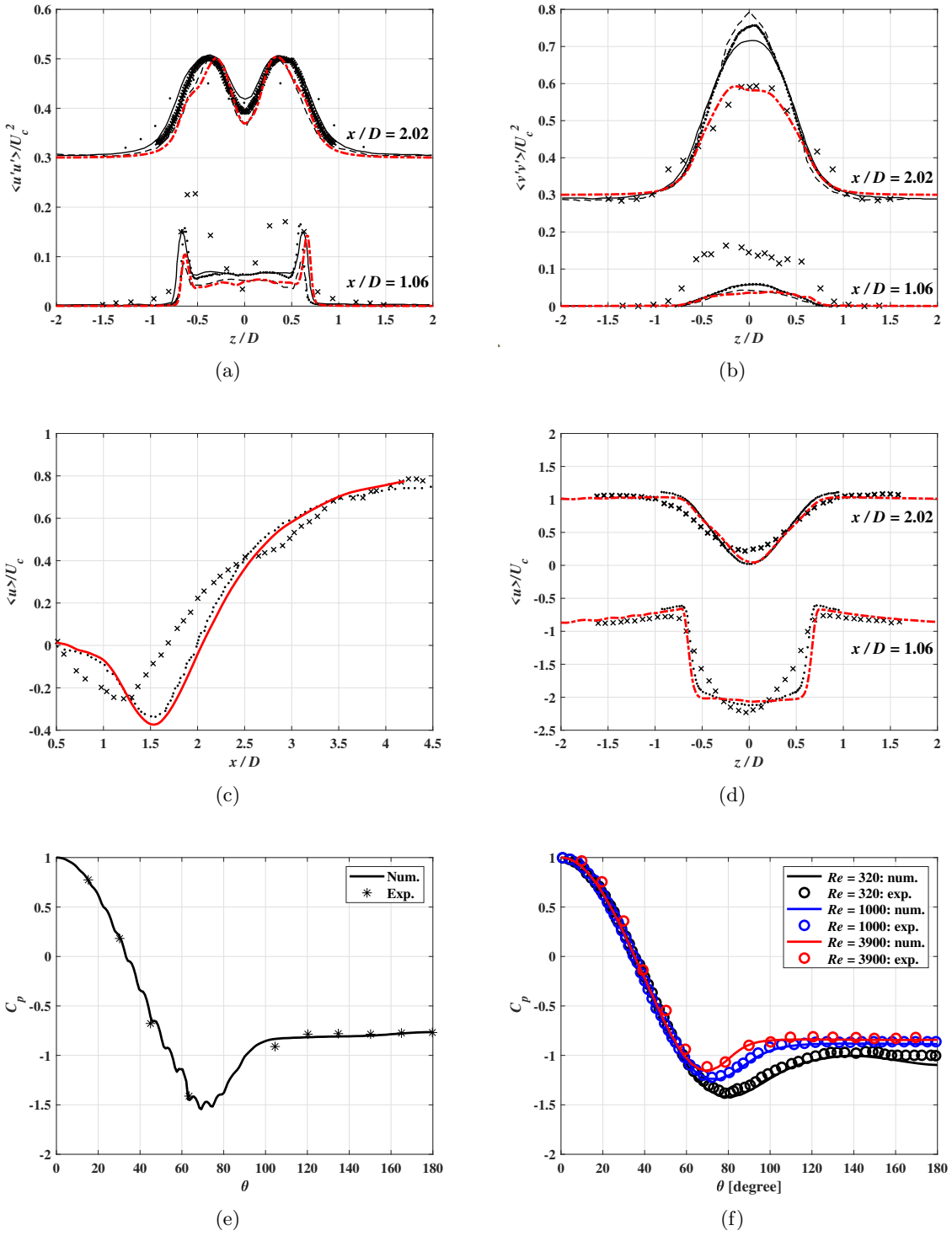

Figure 7: Profiles of the non-dimensional resolved Reynolds stresses (a-b), stream-wise mean velocities in longitudinal and span-wise directions (c-d), the fluctuation of C_p in the circumferential direction for the validation of the roughness wall function (e) and a wide-range of Re (f). (—) LES simulations in Parnaudeau et al. (2008); (• • •) PIV measurements in Parnaudeau et al. (2008); (× × ×) experiments in Lourenco (1994); (- - -) Direct Numerical Simulation (DNS) in Ma et al. (2000); (- . - with red marks) Dynamic subgrid-scale model in this paper; (∘ with black marks) Experimental data in Norberg (2002); (∘ with blue marks) Experimental data in Cao et al. (2010); (∘ with red marks) Experimental data in Norberg (1994).

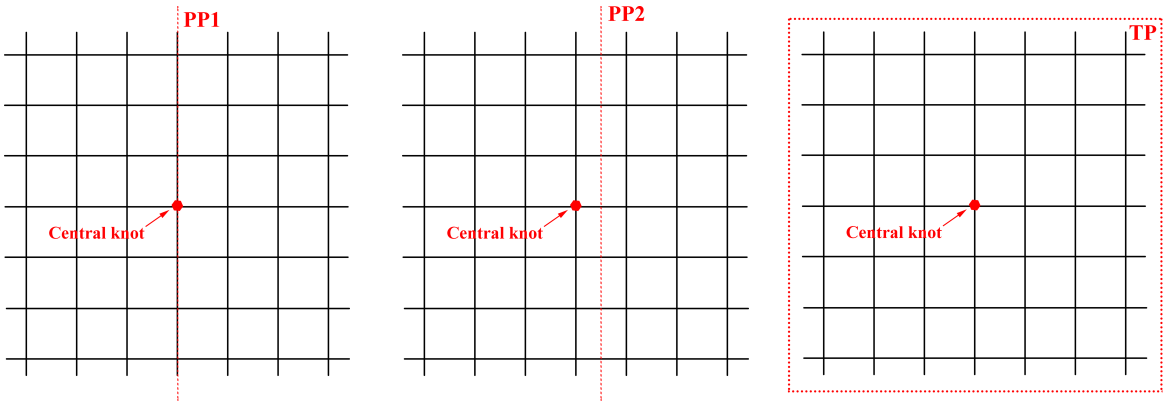

(a) PP1 (b) PP2 (c) TP

Figure 8: Definition of the sampling planes slicing through the net panel.

Additionally, the mean velocity profiles can be conducted for analysing the effects of multiple meshes on the flow patterns. It is seen from Fig. 9a that the area of local acceleration is largest in the mesh closest to the centre of the net panel and smallest in the mesh located in the corner of the panel. Also, the general velocity distribution is central symmetrical to the centre of the panel. Thus, the flow patterns around the central part of the panel are additionally influenced by the surrounding meshes which highlights the importance of investigating net panels with multiple meshes in comparison to previous studies concentrating on a single cruciform Deng et al. (2007)Koide et al. (2017)Zhao and Lu (2018). The influence might be attributed to the additional flow arising from upstream flow reflections from neighbouring cruciforms and twines which lead to the formation of a saddle-back shape around the twines Osaka et al. (1983a).

The hydrodynamic pressure coefficient distributions around the twine circumferences of SN1 and TN1 at P1 and P2 (see Fig. 9c-d for the definition) are analysed in Fig. 10. The LES result obtained by Cao et al. (2010) for a single cylinder at $Re = 1000$ is included as a reference. It can be seen that the pressure distribution around the twisted structure is larger than around a circular cylinder which follows the observed velocities above. Also, the pressure around the P1 section is higher than that around the P2 section in the circular smooth twine, and the latter follows the varying envelope for the isolated circular cylinder. It is related to the influence from the surrounding net meshes, neutralising the hydrodynamic influences as a single cylinder. For TN1, the separation point ranges from $60° - 100°$ which is slightly earlier than for the single circular cylinder ($100° - 120°$) and SN1. The effects are caused by the varying extents of fluid accelerations while passing the meshes for the smooth and twisted structures. This has also been confirmed in the previous sections.

More details are studied by visualising the vortex patterns around P1, P2, P3, and P4 as velocity streamlines around the meshes in Fig. 11. Behind the twisted twines, up to two distinct vortices are observed, whereas up to 6 are visible behind the smooth structure. However, the size of the vortex behind a twisted twine is larger than the vortex street behind a circular cylinder. Moreover, it can be seen that the characteristics of the vortex street vary with the location on the net panel. At the boundary of SN1 (P1 and P3), the vortex behind the cylinder shifts towards the edge of the panel which might be explained by the one-sided

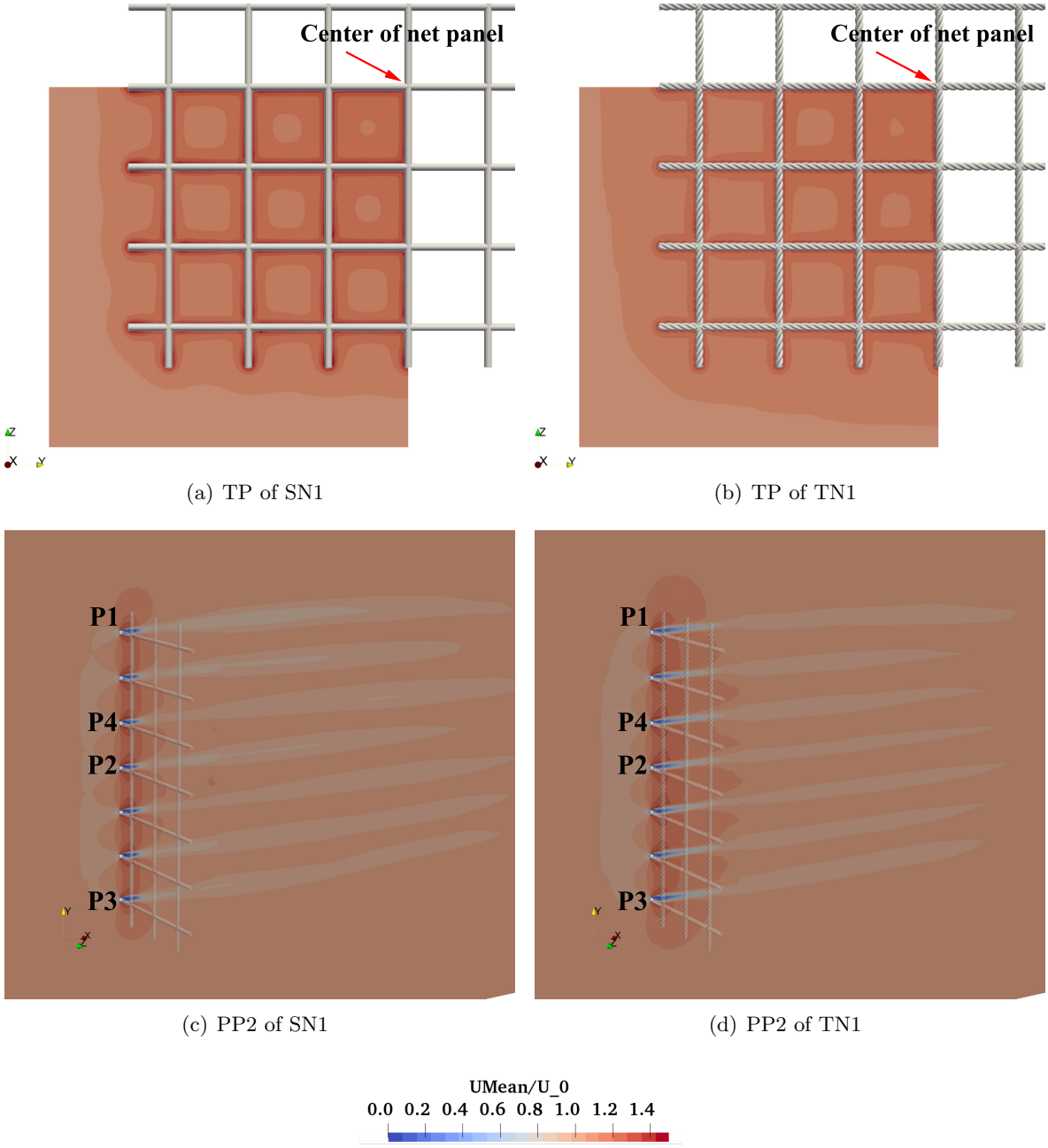

(a) TP of SN1

(b) TP of TN1

(c) PP2 of SN1

(d) PP2 of TN1

Figure 9: $\overline{U}/U_0$ profiles of SN1 and TN1 in TP and PP2. (a) and (b) shows only a quarter of the whole panel due to symmetry.

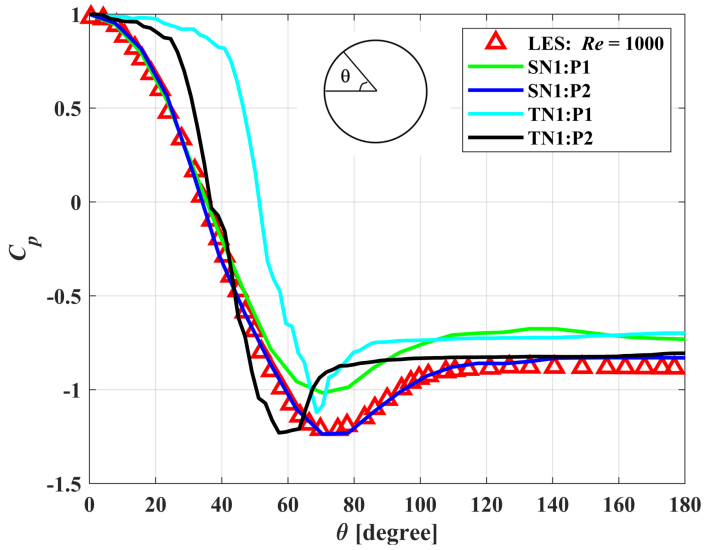

Figure 10: C_p distribution around the twines located at P1 and P2 for SN1 and TN1. Note:"LES: $Re = 1000$" is obtained from LES results in Cao et al. (2010). Here, θ is the angle along the boundary of the cylinder as shown in the figure.

influence from neighbouring meshes. This explanation is confirmed by the observation that the six vortices in P2 of SN1 are fully symmetrical to the x-axis and that no significant difference between P2 and P4 can be seen. In comparison, TN1 shows fewer differences for the vortex patterns with respect to the position of the twine and no significant difference in the width of the recirculation zone. The vortex streets close to the boundary, P1 and P3, are formed from two distinct vortices with an angled symmetry line between them. In the centre of the panel, similar vortices arise with a larger distance to the structure itself. It should be noticed that the cases including twisted material are highly three-dimensional due to the secondary flow induced by the variation of the structural surface at the twine in a third direction Wang et al. (2019). Thus, the flow pattern behind TNs varies significantly in different cross-sections of the twisted twine so that their evaluation is rather complex. It is finally noticed that the observed patterns are similar to those shown for two side-by-side cylinders in Afgan et al. (2011).

Effects of incoming velocity, diameter and length of the twines on the deviation angles Løland (1991) utilised the assumption that the hydrodynamic influence from net meshes on the fluid can be neglected in case of $l/d > 5 - 6$ in order to derive his empirical wake model behind net panels. Consequently, this assumption is studied using the deviation angle at the P1 locations where non-uniform streamline patters are observed. The deviation angles are defined as the angle between the line through the centre of the vortices in the wake of the twine and the horizontal direction (see Fig. 11 SN1: P1 for an illustration). As proved in the above section, it is seen as a measure for increasing influence of the net on the wake behind individual twines and meshes. The variation of the deviation angle is analysed for varying inflow velocities and twine properties (d and l) using all simulations.

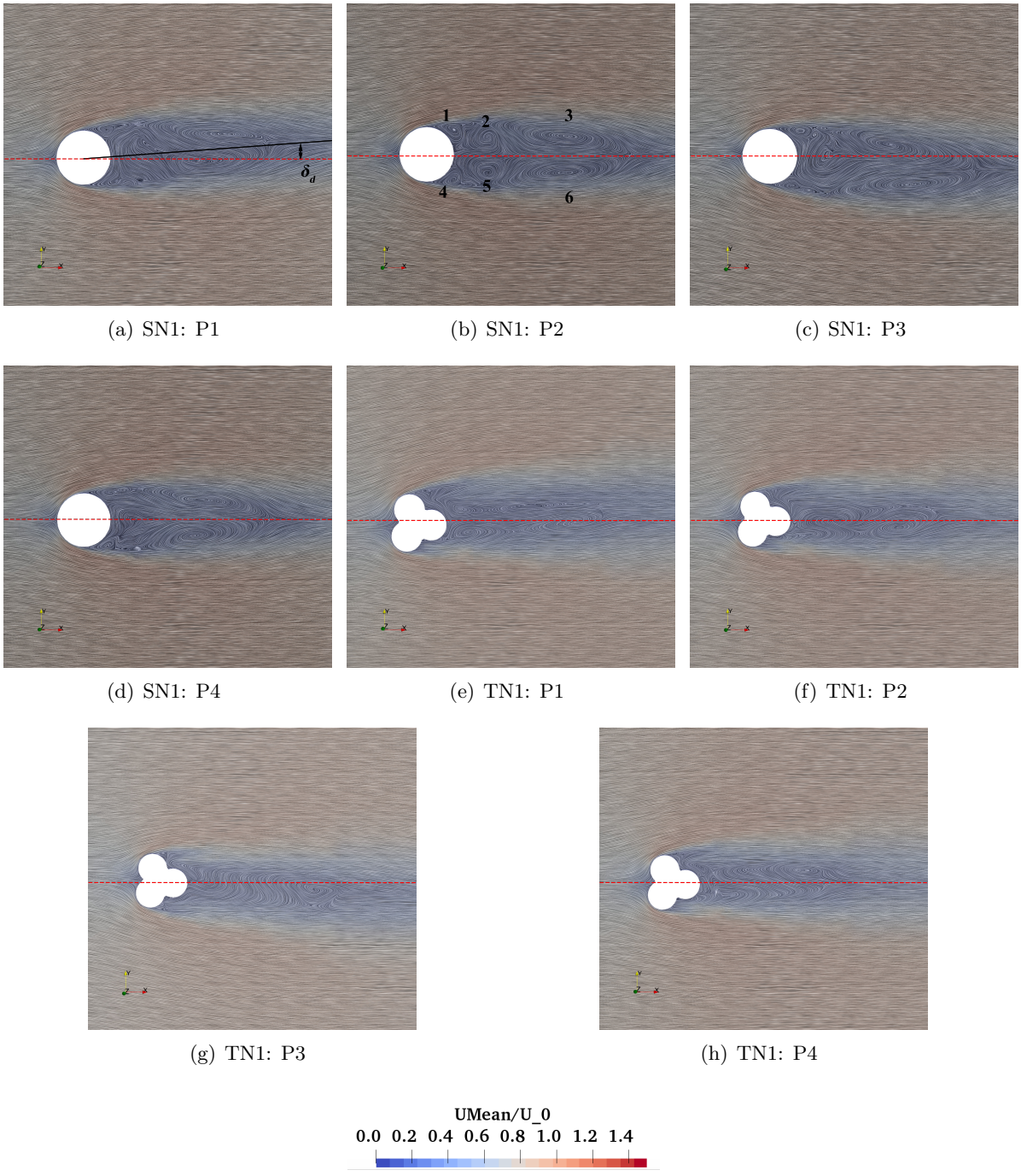

(a) SN1: P1 (b) SN1: P2 (c) SN1: P3

(d) SN1: P4 (e) TN1: P1 (f) TN1: P2

(g) TN1: P3 (h) TN1: P4

Figure 11: Streamlines around individual twines located at P1-P4 for SN1 and TN1. The horizontal red dashed lines represent the centre in the chord-wise direction of the twines. The black solid line in SN1:P1 is the deviation line used in the definition of δ_d.

As shown in Fig. 12, the angles fluctuate marginally with the variation of U_0, but the effects of d and l on the angle are more prominent. Here, the variation of flow regimes from laminar to turbulence cannot affect the flow deviated directions around nets. The angles show a non-linearly increasing trend with an increase of d and decrease of l for SN cases. Both indicate an increased flow disturbance with decreasing distance between the twines. Also, the twisted structures generally tend to produce larger deviation angles. It is however noticed that the variations of d and l lead to different cross-section shapes at the considered section through the twine for TNs. According to Wang et al. (2019), this ultimately influences the expected vortex pattern behind the twine and thus, also the deviation angles. Further comparison is enabled by plotting the data with varying l / d ratio in Fig. 12d. It is obvious that for l/d around 5, the effects due to interacting flow patterns cannot be neglected especially for twisted structures. This contradicts Løland's assumption. Also, the comparison to side-by-side cylinder cases shows a larger l / d range of significant angle deviations due to the enhanced disturbance of the flow through the intersections of the twines in each mesh.

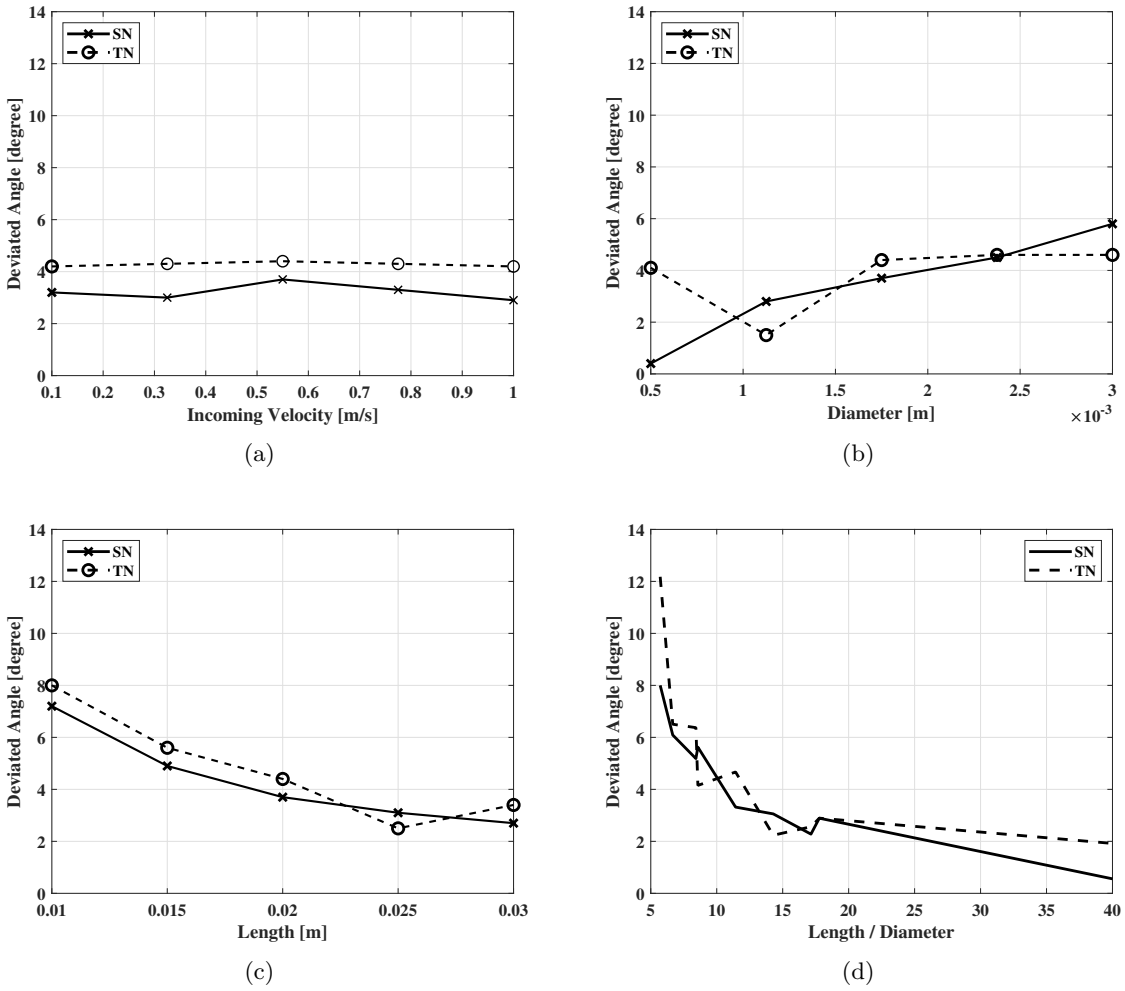

Figure 12: Variation of the deviation angles with respect to U_0, d and l at P1 locations of SN and TN.

Additionally, the variation with respect to U_0, d and l is utilised to express the net influence in terms of the net solidity and the Re. As the result, the parametric scatters for SN and TN are plotted in Fig. 13. Again, the effects of S_n, as a measure of the geometrical properties of the net, are more important than the influence of Re. This confirms the experimental findings of Bi et al. (2013) who concluded that mainly the net solidity affects the fluid velocity distribution in the downstream region of planar net panels.

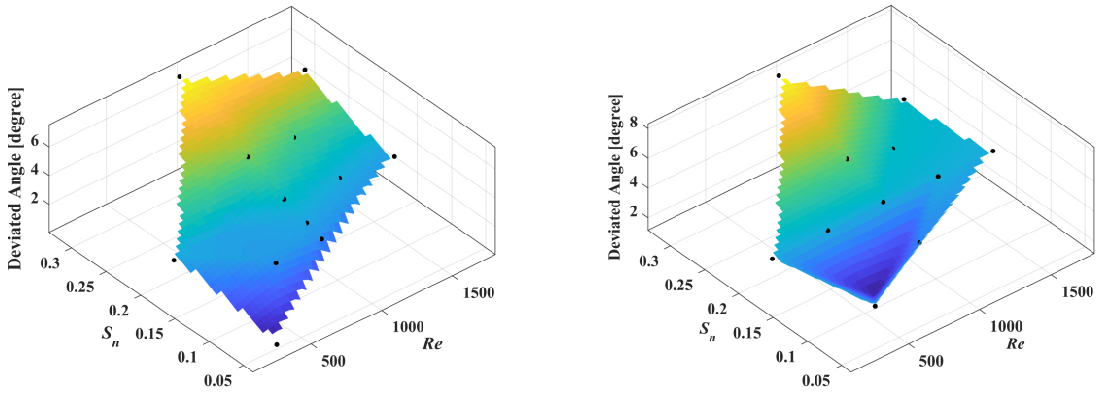

(a) SN (b) TN

Figure 13: Parametric surface representing the deviated angle as a function of Re and S_n for SN and TN. The black dots indicate the actual data points from the simulations.

4.2 Near-field wake

In this section, the turbulence properties of the fluid around the centre part of the net panels, PP1, are discussed in detail. As noted in the PIV experiments of Cha et al. (2013), this zone is the most important region for the development of the wake due to the effects of the fluid-solid interface and turbulent mixing. The PP2 plane is not considered further because of the expected simple flow patterns in the wake close to the twine, which closely coincides with the flow around a circular cylinder as shown in Bi et al. (2017); Wang et al. (2021).

The instantaneous vorticity profiles of SN1 and TN1 in the PP1 plane are presented in Fig. 14. The intersection area has a significant impact on the vorticity field. Also, the region of the area with raised vorticity is larger for the twisted than for the smooth net. Comparing with LES results of a single circular cylinder Henderson (1997) shown in Fig. 14c, more distorted vorticity profiles are visible. Here, the reported phase dislocations along the span of the cylinder are superimposed on the additional vortex induction at the intersections of the twines. As expected, the smooth net results are rather comparable to the single cylinder case than the twisted panel results due to their three-dimensional anisotropic surface structures inducing higher cross-flow velocities alongside the twines.

Fig. 15 presents the three-dimensional vortex profiles around the central mesh of SN1 and TN1. The vortices are visualised as the λ_2 values obtained with Eq. (18). It is shown that Kármán vortices appear in the near-wake region behind the twines in both cases, including the shed shear layers due to the instability as well as the filament-shaped vortices alongside

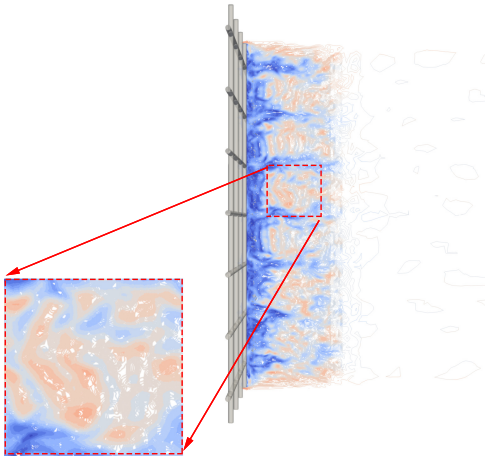

(a) PP1 of SN1

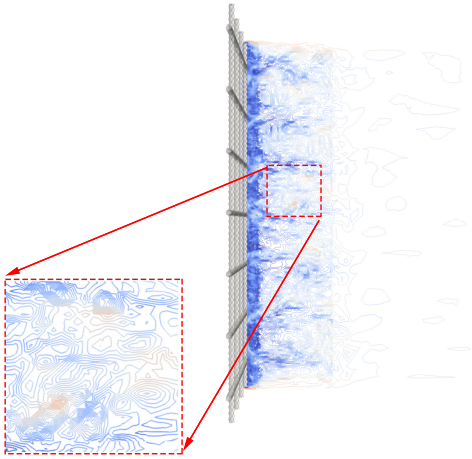

(b) PP1 of TN1

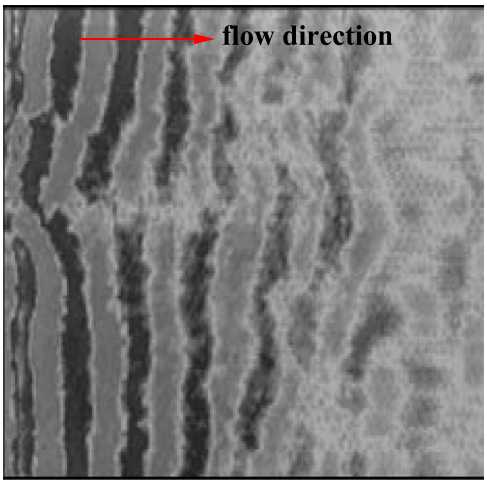

(c) LES in Henderson (1997)

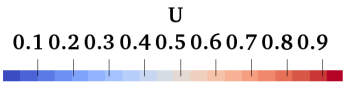

Figure 14: Instantaneous vorticity profiles of SN1 and TN1 in PP1 and PP2. (c) shows one phase of the span-wise turbulent wake behind a circular cylinder at $Re = 1000$ obtained from Henderson (1997).

the shear layers. Comparing Fig. 15a and c, minor distinct differences are visible downstream of the shear layers between SN1 and TN1. According to the three-dimensional PIV measurements of the flow around single cylinders by Scarano and Poelma (2009), the roll-up of the vortices as separated shear layers should be observable at approximately two diameters behind the cylinder axis in the transitional regime. However, this phenomenon is not clearly visible for the smooth material in Fig. 15b. This might be caused by the limited span-wise length of the twine with increased flow disturbance at the intersections. In comparison, the separated shear layers of TN1 elongate further into the wake region (Fig. 15d). This difference between twisted and smooth cylinders is in accordance with other computational studies on single twisted cylinders Jung and Yoon (2014). In addition, Fig. 15c reveals that the shear layers separate in a waved pattern from the twisted twines resulting in a wake pattern of multiple hair-pin vortex filaments, and the extension of the free shear layers which are impacted by the concave-convex structures.

Next, the TKE in the region close to the net is analysed to quantify the turbulence intensity Puzdrowska and Heese (2019)Yue et al. (2015), composed of the resolved and modelled part from the LES results. First, the TKE distributions on the PP1, PP2 and multiple transversal slices behind SN1 and TN1 are shown in Figs. 16 and 17. The distributions of TKE on PP1 and PP2 indicate a significant difference in the distribution and strength of the turbulence in the different segments of a finite net panel. The maximum energy is expected behind the individual twines and especially, on both sides of the intersections. The variation of TKE is also stronger in the PP1 slice than in the PP2 slice indicating that the turbulent flow fluctuations in the span-wise direction of the twines are more intensive than around the stream-wise directions. Additionally, the TKE is rather small in the voids between the meshes as shown in Fig. 16b. In comparison to SN1, the turbulence fluctuations for TN1 reach similar into the wake but are generally lower in magnitude, and this is also confirmed in Fig. 17. Jung and Yoon (2014) additionally reported periodic variations of TKE along the span-wise direction of a single twisted cylinder. This phenomenon cannot be seen here, probably due to the finite length of twines and the relevance of the intersections. The analysis of the TKE distribution in the transversal slices (Fig. 17) reveals that the maximum TKE of SN1 and TN1 occurs at approximately $x/l = 1/2$ and $x/l = 1/4$ behind the panel, respectively. Behind this point, the energy declines to a minimum when approaching the far-field region at $x/l = 4$. This is consistent with the conclusion that the TKE fluctuations appear mainly behind the twines and cruciforms.

Further insight is provided by analysing the resolved Reynolds stresses along two probe lines cutting the PP2 plane at $x/d = 6$ and $x/d = 7$ (Fig. 18). The Reynolds stresses in the wake of a single circular cylinder using LES Cao et al. (2010) are shown for comparison. With the increase of x/d, both magnitudes of the stream-wise and shear Reynolds stresses decrease for SN1 but no discrepancy can be noticed for TN1. The stream-wise Reynolds stresses are distributed for both materials differently, wherein the dissipations of turbulence stresses of TN1 are more considerable than for SN1 and the isolated circular cylinder case. Furthermore, two distinct stress peaks are observed on both sides of smooth twines, and the peaks are not axis-symmetrical except for the central twine. But, these phenomena are not visible for the twisted configuration which is attributed to the impacts of the concave-convex surface structures. Additionally, it is determined that the stream-wise Reynolds stresses around the central smooth twine are closer to the results from the single circular cylinder. In contrast to that, the magnitudes of the shear stress across the middle twines of SN1 are significantly

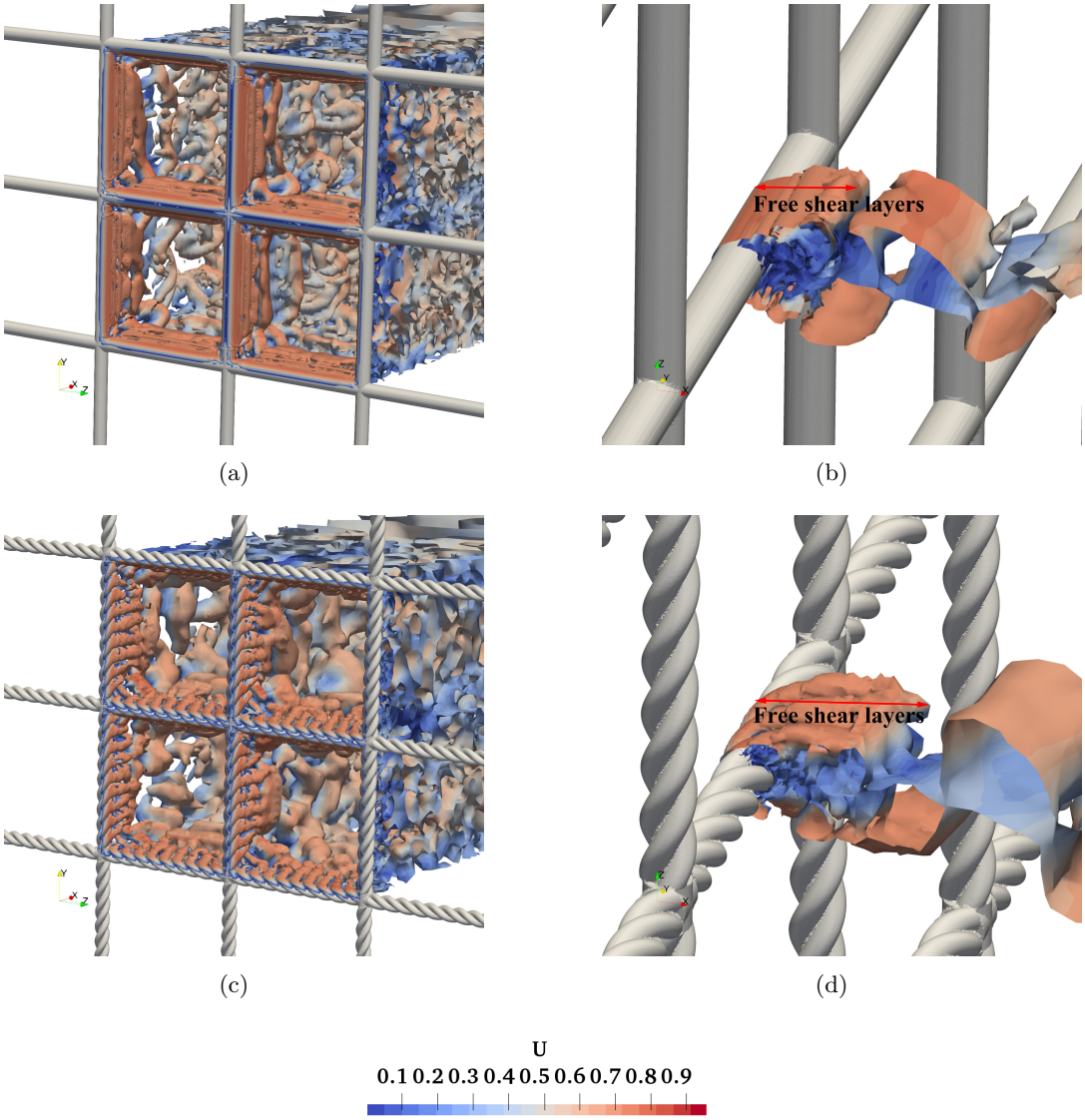

(a) (b) (c) (d)

Figure 15: Iso-surfaces of the negative λ_2 values around the central net mesh of SN1 (a-b) and TN1 (c-d).

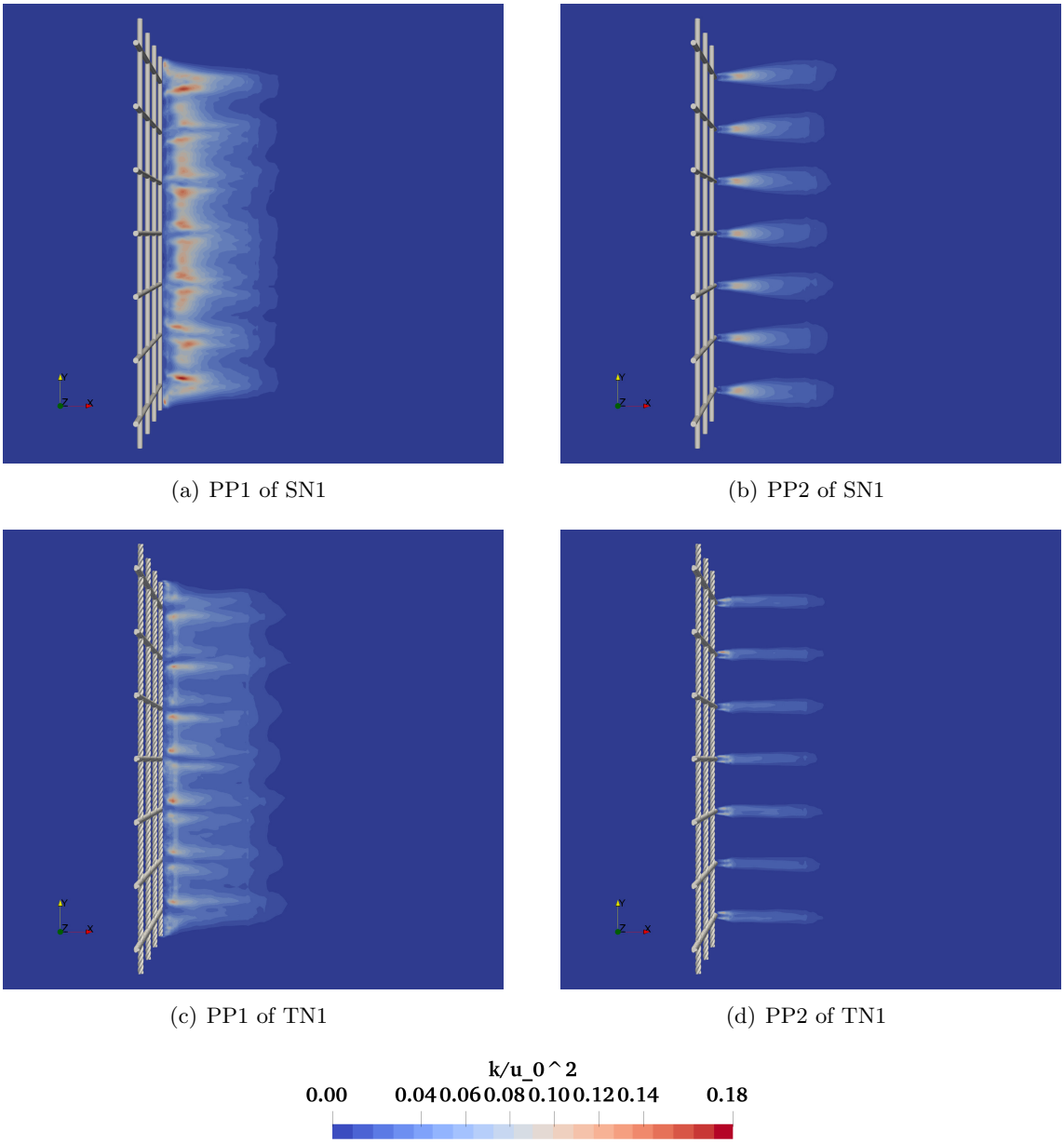

(a) PP1 of SN1

(b) PP2 of SN1

(c) PP1 of TN1

(d) PP2 of TN1

Figure 16: Non-dimensional TKE profiles of SN1 and TN1 in PP1 and PP2.

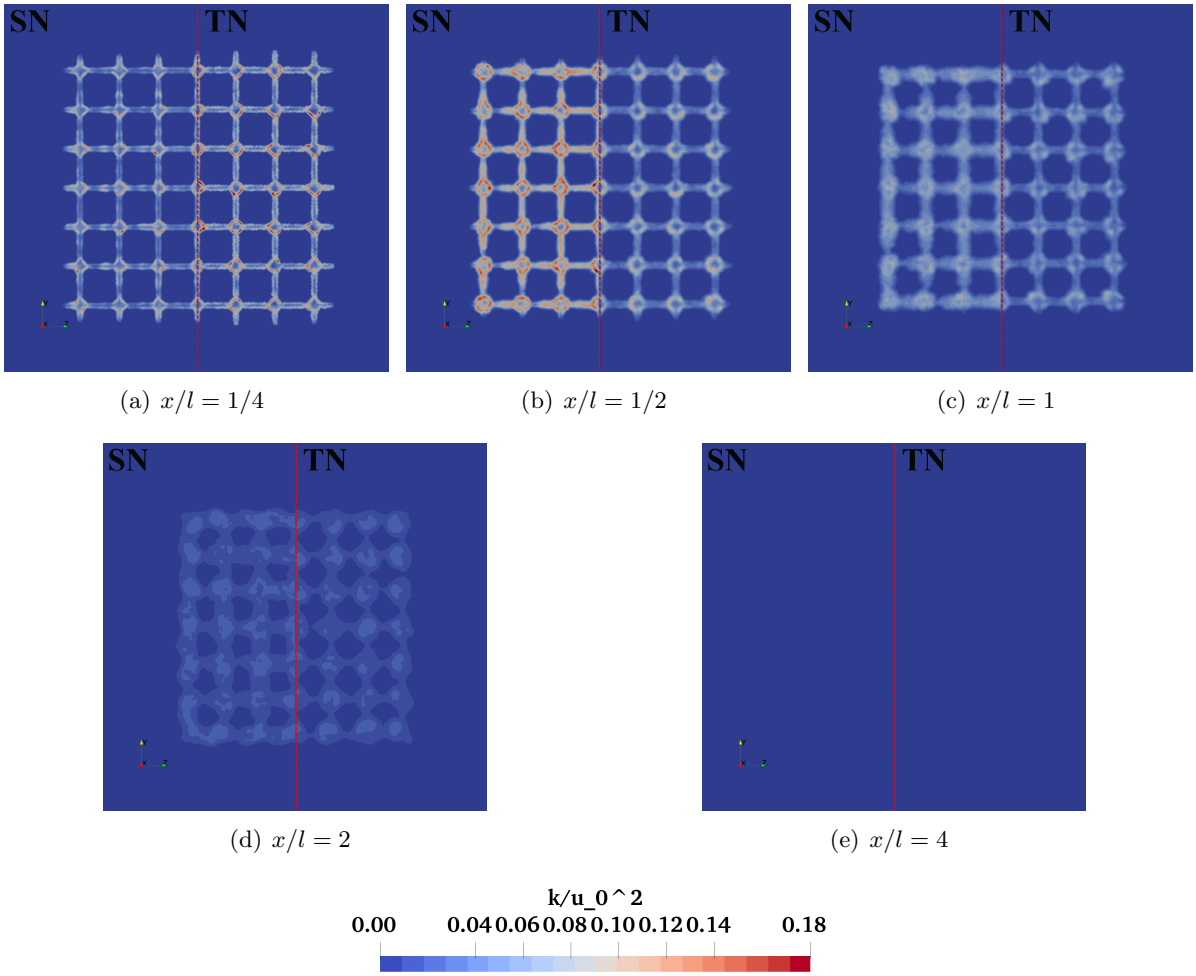

(a) $x/l = 1/4$ (b) $x/l = 1/2$ (c) $x/l = 1$

(d) $x/l = 2$ (e) $x/l = 4$

Figure 17: Non-dimensional TKE profiles of SN1 and TN1 in transversal slices in the near-field wake region. Only one half of the net is shown in each of the two cases due to symmetry. The red dashed line in (b) indicate the probe line 2 used in section 4.2.1.

larger. TN1 generally predicts smaller stream-wise stresses which is caused by the reduced velocity fluctuations close to the net in comparison to SN1, and it is also depicted that the twisted cylindrical structures show a minor influence on the shear stress distributions from Fig. 18d.

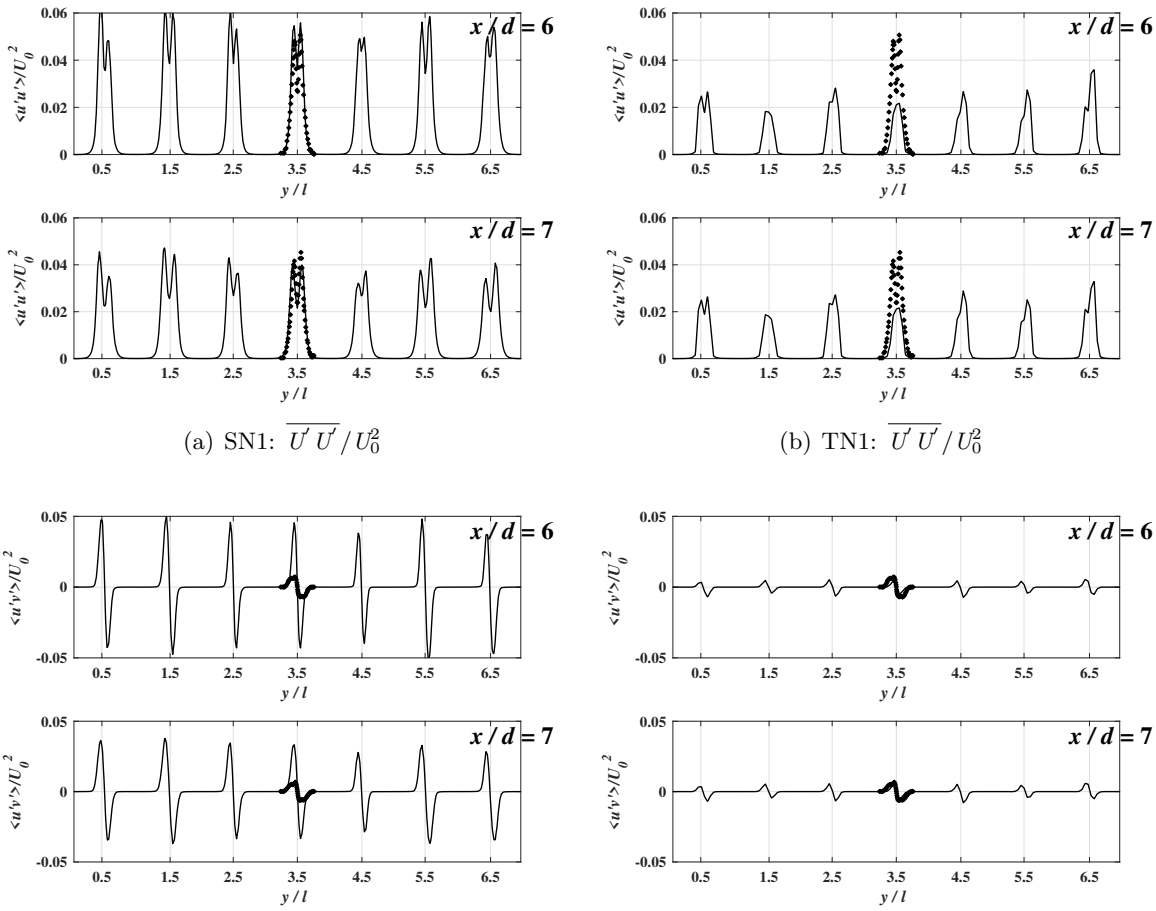

(a) SN1: $\overline{U'U'}/U_0^2$ (b) TN1: $\overline{U'U'}/U_0^2$

(c) SN1: $\overline{U'V'}/U_0^2$ (d) TN1: $\overline{U'V'}/U_0^2$

Figure 18: Distribution of the mean resolved stream-wise and shear Reynolds stress components along probe lines cutting PP2 at two x/d locations. Data with the diamond symbol represents results of the LES in Cao et al. (2010).

Effects of incoming velocity, diameter and length of the twines on the TKE The relation between the distribution of the TKE and the parameters U_0, d and l is investigated next. For this purpose, two probe lines are introduced to capture the turbulence fluctuations around the net panels. The first probe line (Probe 1) is located along the x-axis through the centre intersection of the panel and the second probe line (Probe 2) points in y-direction at $x/l = 1/2$ behind the net as illustrated in Fig. 17b. The resulting distributions for the different configurations are presented in Fig. 19.

The distributions of the TKE in stream-wise direction indicate low turbulence intensities

in front of the net panels as well as in the very far-field region behind them. In between, the energy first rises sharply while passing through the structure and then gradually reduces. Besides, the TKE fluctuates along the second probe line every time a twine or intersection is passed by the probe. It is further noticed that the energy along the two probe lines as well as the length of the influenced zone increases mostly with increasing d and increases just slightly with the inflow velocity. The twine length seems to have no significant effect on the turbulence fluctuations across Probe 2, whereas that in the stream-wise direction are correlated with l. This indicates that the TKE is rather determined by Re than by the solidity of the net. Similar to the figures above, this finding is less significant for the twisted material cases due to a generally smaller TKE.

4.3 Velocity reduction in the far-field wake

Finally, the very far-field wake regions for SN1 and TN1 are analysed using the normalised mean velocity distributions obtained from slices at $x/d = 20$ so that eventual influences from the outlet boundary are avoided (see Fig. 20). This will ultimately lead to the velocity reduction analysis behind net panels and the development of a more reliable formula for evaluating the effect of nets on the fluid in simulations including full-scale net panels, fish cage arrays or tandem net planes Bi et al. (2013). It is first to be noticed that the fluid velocity reduction is present for both materials. Generally, multiple peaks and valleys are observable in accordance with the arrangement of the different twines, but strong three-dimensional flow patterns lead to a mixing of the near-field wake velocities. The velocity reduces to $85\% - 95\%$ of the inflow velocity for both twines, while the local accelerations along the voids in twisted twines are more apparent. By comparing Fig. 20a and b, it can be seen that the influence area for TN is slightly larger than that for SN. Based on these findings, the conclusion of Klebert et al. (2013), that the wake is not the simple addition of perpendicular wakes behind multiple cruciforms, can be confirmed numerically.

The study is further extended by including all different configurations of the smooth net panel. Hence, the very far-field wake profiles can be analysed as functions of d and l of the twines. The resulting distributions are presented in Fig. 21. The further analysis of varying U_0 is not included as the investigated range of velocities do not influence the results for the relative velocity reduction in the far-field. Also, the twisted configurations are not included in this analysis because the distribution of the velocities in the far-field wake mostly coincide with the smooth net cases (compare Fig. 20). It can be generally seen from Fig. 21 that the material properties, d and l, significantly influence the variation of the fluid velocity behind net panels. This again validates the conclusions of Bi et al. (2013), that the solidity of nets is the main factor affecting the downstream velocity field. Furthermore, no obvious velocity reduction is observed for SN6 due to the small solidity of $S_n = 0.049$ except for the considerable local velocity acceleration around the net centre. Also, a notable increase of velocity reduction is revealed with increasing d and decreasing l, which relates to a higher solidity. Here, the scattered pattern of velocity reduction converges to a more continuous area of decelerated flow with increasing S_n. This is particularly visible for SN10. At the same time, areas of locally accelerated fluid arise close to the outer edges of the net panels with increasing d and decreasing l. This is caused by the reduced porosity turning the net panel into a bluff body, which can also be observed in SN9 and SN10.

Based on these results, a quantification of the velocity reduction in the far-field downstream

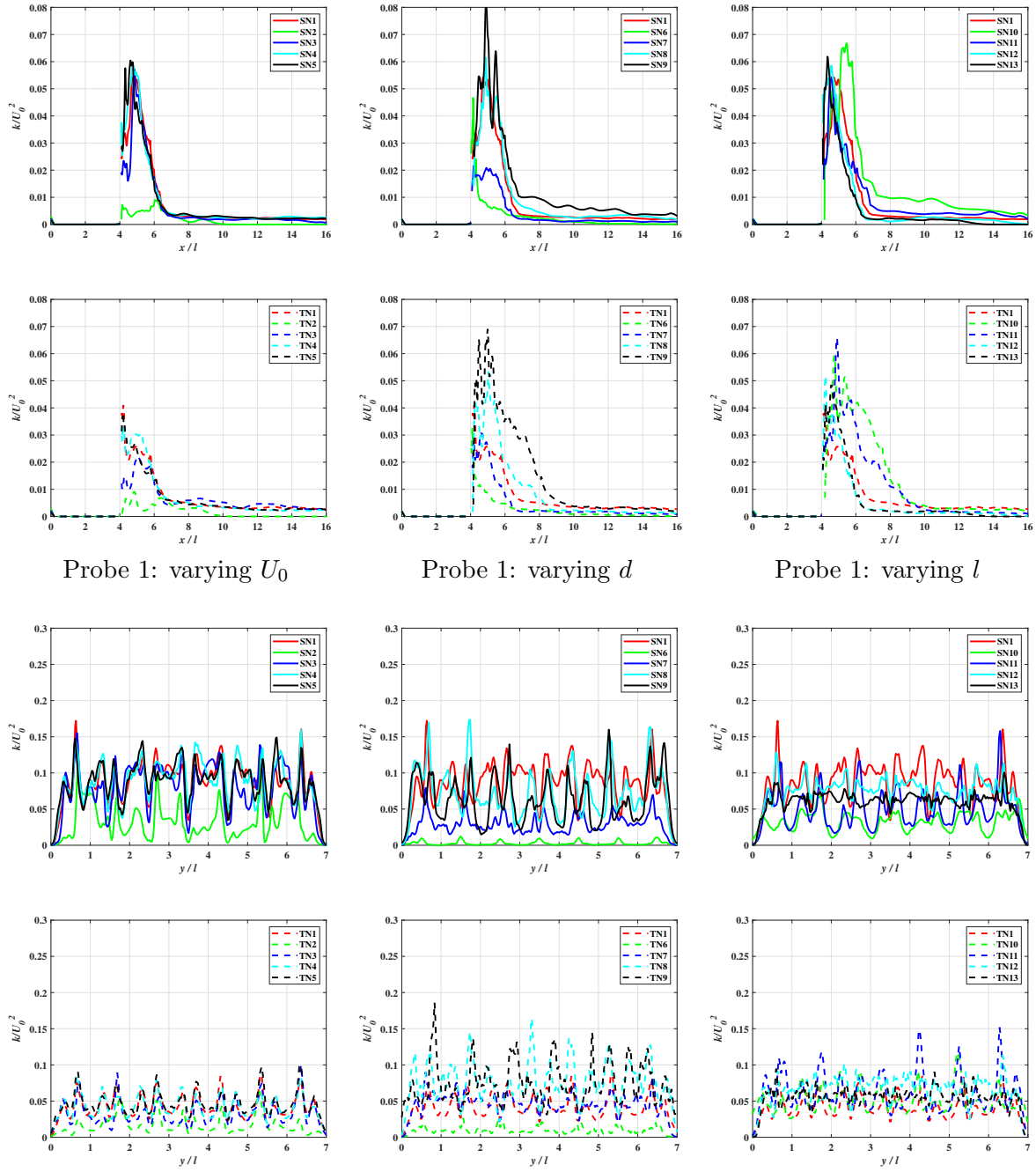

Probe 1: varying U_0 | Probe 1: varying d | Probe 1: varying l

Probe 2: varying U_0 | Probe 2: varying d | Probe 2: varying l

Figure 19: Distribution of the non-dimensional TKE along two probe lines for the various SN and TN cases. See Tab. 1 for detailed information of each case and Fig. 17 for the definition of the probe lines.

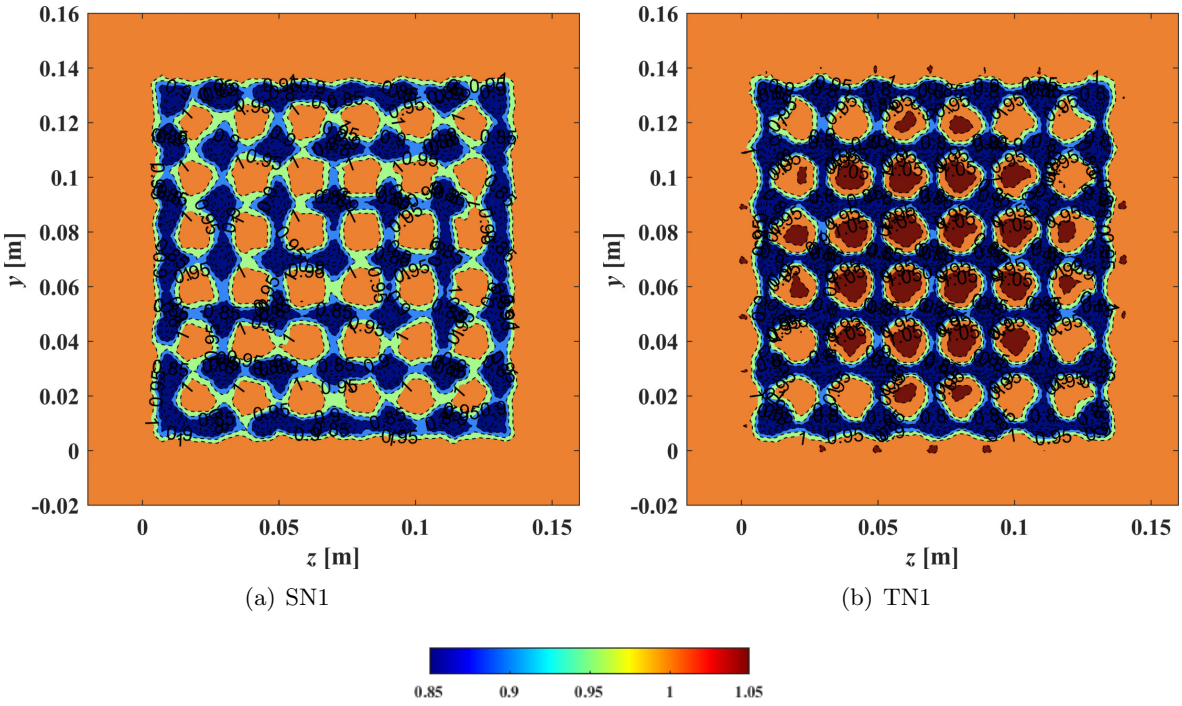

(a) SN1 (b) TN1

Figure 20: $\overline{U}/U_0$ profiles for SN1 and TN1 in slices at $x/d = 20$.

of net panels is proposed. For this purpose, the Area-Averaged Velocity Reduction ($AAVR$) is introduced. It is defined as

$$AAVR = \frac{\int_A (\overline{U}/U_0)_{\text{cell}} \, \mathrm{d}A}{A}, \tag{19}$$

with A the cross-sectional area of the net panel and $(\overline{U}/U_0)_{\text{cell}}$ the non-dimensional mean velocity in the cell centre next to the corresponding portion of the area. Thus, the velocity reduction is estimated considering the weight of each computational cell. This is a more realistic presentation of this quantity compared to the commonly applied velocity reduction factor assuming a constant velocity reduction in the wake. The results for $AAVR$ with varying U_0, d and l are shown in Fig. 22. The empirical linear relation between the velocity reduction factor and C_d from Løland (1991) is taken as a reference. Here, C_d is calculated with Eq. (16) based on the CFD simulations.

It is demonstrated that the velocity reduction of TNs is marginally larger than for SNs. The wake model of Løland (1991) predicts larger velocity reductions by $3 - 10\%$ among all cases. With the increase of the incoming velocity, the $AAVR$ increases slightly for low velocity cases but remains constant at larger velocities. This is in accordance with the findings in Tu et al. (2020). The velocity reduction further increases with a larger d and smaller l of the twines, and the difference to the empirical formula raises simultaneously. This indicates the largest discrepancy appears for the largest solidity cases. Based on these observations, first-order polynomial regression is used to fit the simulated data for the velocity reduction of all SNs and TNs. The resulting formulae Eq. (20)$\sim$(21) have a goodness of fits of approximately

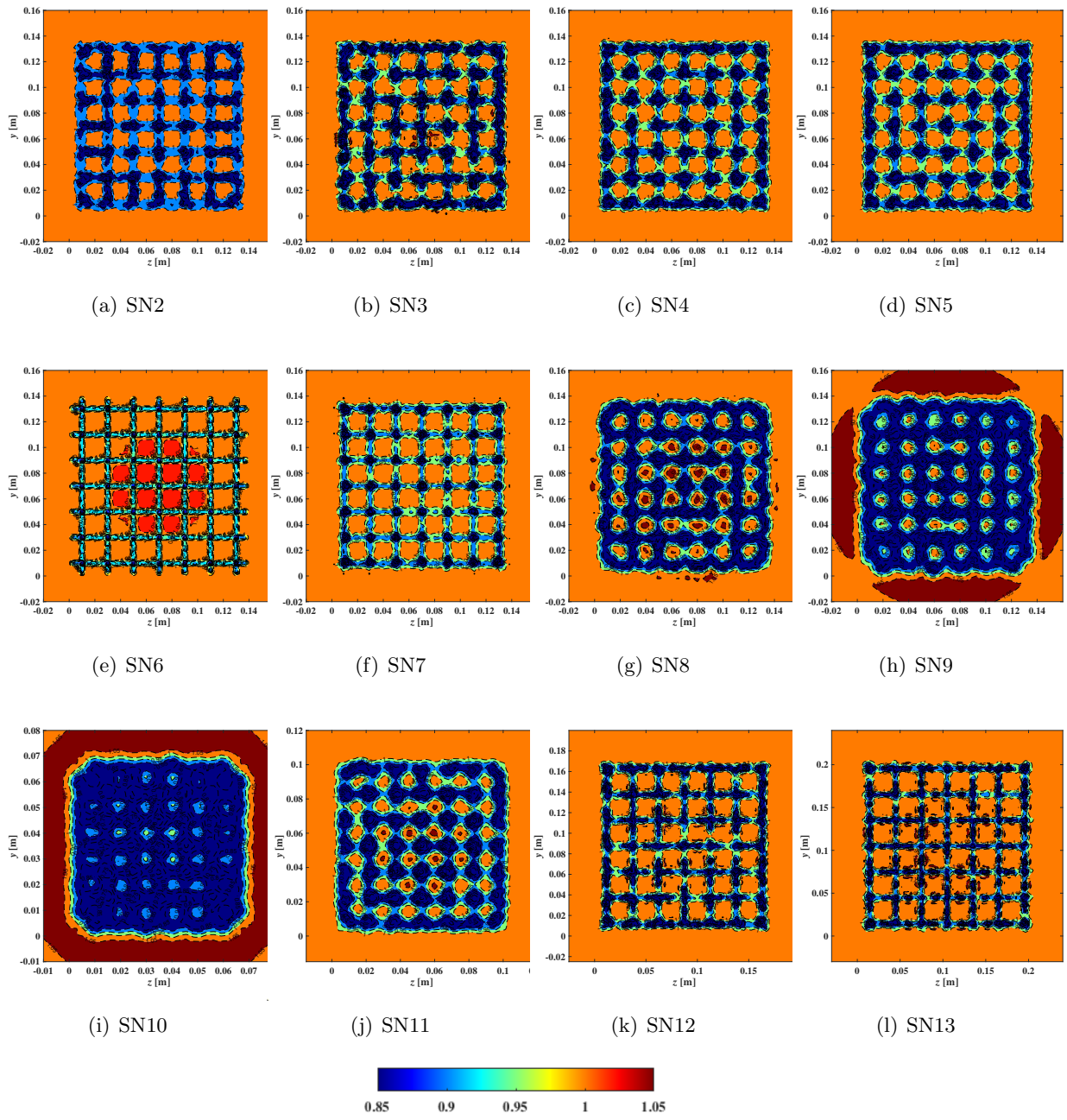

(a) SN2 (b) SN3 (c) SN4 (d) SN5

(e) SN6 (f) SN7 (g) SN8 (h) SN9

(i) SN10 (j) SN11 (k) SN12 (l) SN13

Figure 21: $\overline{U}/U_0$ profiles for all SN cases. See Tab. 1 for more information of each SN case. The length and width of the analysed area is extended outwards by one l.

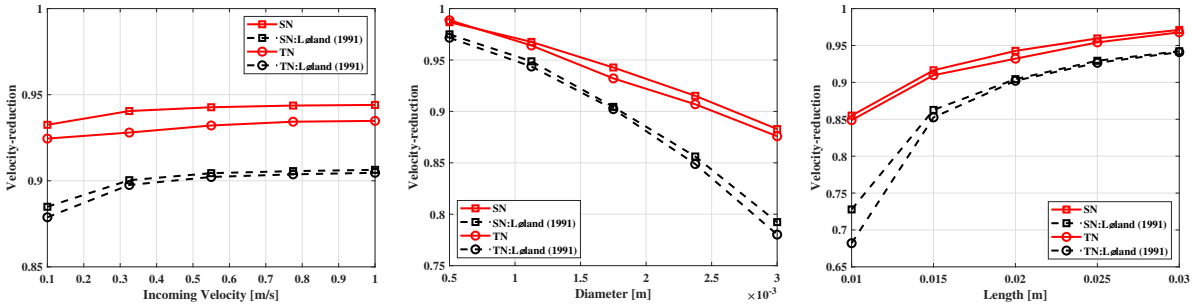

(a) (b) (c)

Figure 22: Distribution of the velocity reduction factor with varying U_0, d and l for SN and TN in comparison to the wake model in Løland (1991). The red solid lines denote the simulated results while the black dashed lines are from the analytical formula of Løland (1991).

97.3% which is assumed to be a reliable quantification for the velocity reduction behind net panels. The arising simulation-based formulae stand in contrast to the existing empirical approaches based on theoretical derivations with strong assumptions. Generally, $AAVR$ is more sensitive to changes in the solidity ratio of the net than to changing Re Tu et al. (2020). This is also indicated in Fig. 23 where the obtained polynomials are plotted as parametric surfaces with respect to S_n and Re.

$$AAVR_{SN} = (9.1 \times 10^{-6})Re - 0.5327S_n + 1.021, \tag{20}$$

$$AAVR_{TN} = (6.8 \times 10^{-6})Re - 0.5394S_n + 1.016, \tag{21}$$

$$\text{for } (172.97 \leq Re \leq 1729.73, \quad 0.049 \leq S_n \leq 0.319).$$

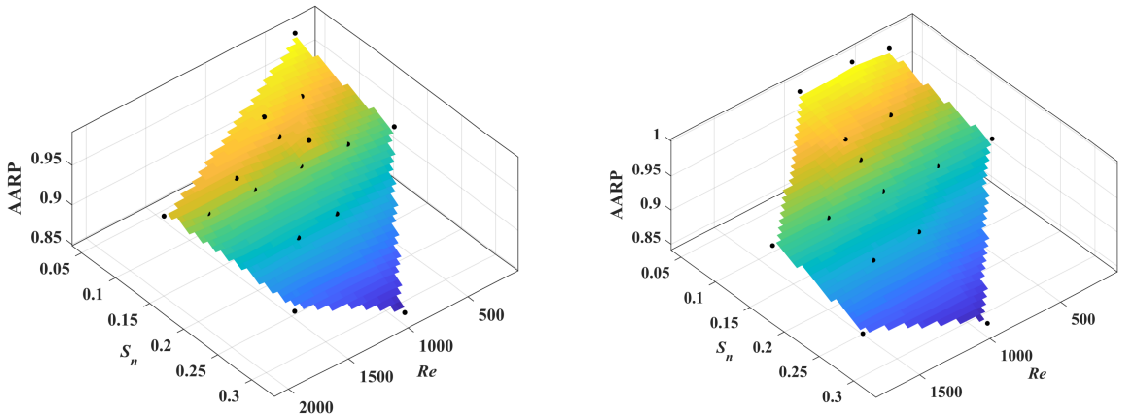

(a) SN (b) TN

Figure 23: Parametric surfaces of $AAVR$ as functions of Re and S_n for SN and TN.

The accuracy of the proposed formula for twisted twines (Eq. (21)) is analysed in Tab. 4 by a comparisons to measured velocity reduction factors behind single and multiple nets. The velocity reductions behind polyethylene (PE) plane nets are obtained from PIV measurements Bi et al. (2013) and evaluated from the time-averaged velocities in the central area of the far-field region. The theoretical velocity reduction model from Løland (1991) is not applicable due to the unknown hydrodynamic loadings for the nets in Bi et al. (2013). For the single net cases, deviations of less than 3% between the proposed model and the experiments are observed. It is to be noticed that the proposed formula predicts a reduction of the velocity reduction with increasing Re which is in accordance with the experiments. In a second experiment, four net panels were placed behind each other, and the velocity was measured between each net as well as behind the last panel. It is expected that the velocity reduces consequently with the number of passed nets. This tendency is well captured by the $AAVR$. Here, the model slightly over-predicts the measured velocities behind the first two panels by only 1% and under-predicts the velocity behind the last panel by up to 9%.

Table 4: Comparisons of the velocity reduction behind plane net panels with the experiments in Bi et al. (2013). For multiple plane net cases, the number in brackets indicates the number of nets passed by the fluid before the velocity is measured. The Re is determined using the reduced velocity prediction behind the previous net.

	Net	Re	S_n	**Velocity reductions**	
				$AAVR_{TN}$	**Experiments**
Single plane nets	N1	290.89	27.20%	0.871	0.859
	N1	437.62	27.20%	0.872	0.861
	N1	581.78	27.20%	0.873	0.880
	N2	290.89	24.30%	0.887	0.901
	N2	437.62	24.30%	0.888	0.910
	N2	581.78	24.30%	0.889	0.911
Multiple plane nets	N2(1)	437.62	24.30%	0.888	0.894
	N2(2)	397.24	24.30%	0.788	0.790
	N2(3)	360.49	24.30%	0.699	0.742
	N2(4)	327.06	24.30%	0.620	0.683

5 Conclusions

In this paper, a study of the flow around the meshes of a net panel with smooth and twisted 3-ply material was presented using dynamic subgrid-scale large eddy simulations. The specific computational grid resolutions and domain sizes were determined using convergence tests. Then, the numerical solver was successfully validated against measurements of the flow around a circular cylinder and hydrodynamic loadings on net panels. The conclusions of this paper are drawn as follows:

- The analysis of the mean quantities such as velocity and pressure distributions revealed increasing influence on the flow patterns closer to the centre of the panel. The diameter and length of the twines have a crucial impact on the predicted flow pattern due to the deviation angle of the vortex street. In contrast to side-by-side cylinders, the interplay of multiple net meshes reduce significantly once the diameter-length ratio is larger than 20. Further, important differences between smooth and twisted net material were discussed.

- The near- and far-field wake region behind the net panel was investigated in terms of turbulence properties. It is shown that the recirculation zones differ in appearance and length for twisted and smooth twines. The distribution of the turbulent kinetic energy and Reynolds stresses revealed that turbulence fluctuations appear mainly behind the individual twines and the intersections. Here, the diameter is a more important factor for the magnitude of the turbulent kinetic energy than the length of the twines.

- The chaotic velocity patterns in the far-field region indicated strong mixing of the fluid in the wake. A more accurate quantification of the momentum loss behind nets, Area-Averaged Velocity Reduction ($AAVR$), is proposed as new empirical expressions for smooth and twisted 3-ply nets. The solidity of the net was thereby the main factor for increased velocity reduction, whereas the Reynolds number had less influence. The accuracy of the proposed formulae are accessed by comparing to PIV measurements of the flow behind single and multiple plane nets.

The results of the presented studies can now be used to develop additional terms for describing the turbulence distribution through nets in typical RANS models. This can enhance their capability to predict a more realistic velocity field in the wake of nets. It has been concluded in Bi et al. (2017) and Endresen et al. (2013) that the flow around and wake behind nets is also closely associated with the angle of attack. The introduction of this parameter into the CFD studies will be part of further research. Finally, the inclusion of the structural response of the net panel due to the flexibility of the material might be of interest. The main challenge will thereby be the conservation of a high-quality grid during the deformation of the structure. This could be either solved using dynamic mesh strategies or immersed boundary methods, at which at least the latter will compromise the grid resolution in the viscous sub-layer around the twines.

Acknowledgment

The study is supported by the National Key R & D Program of China (No. 2019YFD0901000) and Fund CAFS (No. 2019HY-XKQ03), Research Council of Norway under the HAVBRUK2 project (No. 267981), and the State Foundation for Visiting Ph.D. student from China Scholarship Council (No. 201906330049). This research was supported in part with computational resources at NTNU provided by The Norwegian Metacenter for Computational Sciences (NOTUR, http://www.notur.no) under project No. NN2620K, and the Center for High Performance Computing and System Simulation, Pilot National Laboratory for Marine Science and Technology (Qingdao).

References

Adrian, R.J., Friedrich, R. and Nieuwstadt, F.T. (1994). Fully developed turbulent pipe flow: A comparison between direct numerical simulation and experiment. *J. Fluid Mech.*, **268**, 175–210. 10.1016/j.oceaneng.2021.10984610.1017/S002211209400131X.

Afgan, I., Kahil, Y., Benhamadouche, S. and Sagaut, P. (2011). Large eddy simulation of the

flow around single and two side-by-side cylinders at subcritical Reynolds numbers. *Phys. Fluids*, **23**, 075101. 10.1016/j.oceaneng.2021.10984610.1063/1.3596267.

Arne, F. (2005). *Current Forces on Net Structure*. Ph.D. thesis, NTNU,Trondheim.

Balash, C., Colbourne, B., Bose, N. and Raman-Nair, W. (2009). Aquaculture net drag force and added mass. *Aquacult. Eng.*, **41**(1), 14–21. 10.1016/j.oceaneng.2021.10984610.1016/j.aquaeng.2009.04.003.

Batham, J.P. (1973). Pressure distributions on circular cylinders at critical Reynolds numbers. *J. Fluid Mech.*, **57**(2), 209–228. 10.1016/j.oceaneng.2021.10984610.1017/S0022112073001114.

Beaudan, P. and Moin, P. (1994). Numerical experiments on the flow past a circular cylinder at sub-critical Reynolds number. NASA STI/Recon Technical Report N.

Bi, C.W., Balash, C., Matsubara, S., Zhao, Y.P. and Dong, G.H. (2017). Effects of cylindrical cruciform patterns on fluid flow and drag as determined by CFD models. *Ocean Eng.*, **135**(March 2016), 28–38. 10.1016/j.oceaneng.2021.10984610.1016/j.oceaneng.2017.02.032.

Bi, C.W., Zhao, Y.P., Dong, G.H., Xu, T.J. and Gui, F.K. (2013). Experimental investigation of the reduction in flow velocity downstream from a fishing net. *Aquacult. Eng.*, **57**, 71–81. 10.1016/j.oceaneng.2021.10984610.1016/j.aquaeng.2013.08.002.

Brørs, B. (1999). Numerical modeling of flow and scour at pipelines. *J. Hydraul. Eng.*, **125**(5), 511–523. 10.1016/j.oceaneng.2021.10984610.1061/(asce)0733-9429(1999)125:5(511).

Cao, S., Ozono, S., Tamura, Y., Ge, Y. and Kikugawa, H. (2010). Numerical simulation of Reynolds number effects on velocity shear flow around a circular cylinder. *J. Fluids Struct.*, **26**(5), 685–702. 10.1016/j.oceaneng.2021.10984610.1016/j.jfluidstructs.2010.03.003.

Cha, B.J., Kim, H.Y., Bae, J.H., Yang, Y.S. and Kim, D.H. (2013). Analysis of the hydrodynamic characteristics of chain-link woven copper alloy nets for fish cages. *Aquacult. Eng.*, **56**, 79–85. 10.1016/j.oceaneng.2021.10984610.1016/j.aquaeng.2013.05.002.

Deng, J., Ren, A.L. and Shao, X.M. (2007). The flow between a stationary cylinder and a downstream elastic cylinder in cruciform arrangement. *J. Fluids Struct.*, **23**(5), 715–731. 10.1016/j.oceaneng.2021.10984610.1016/j.jfluidstructs.2006.11.005.

Edwin, L., Thomas, S.N., Remesan, M.P., Ashraf, P.M., Baiju, M.V., Lekshmi, N.M. and Madhu, V.R. (????). ICAR Winter School Manual-Responsible Fishing: Recent Advances in Resource and Energy Conservation. Website.

Endresen, P.C., Føre, M., Fredheim, A., Kristiansen, D. and Enerhaug, B. (2013). Numerical modeling of wake effect on aquaculture nets. In: *Proceedings of the International Conference on Offshore Mechanics and Arctic Engineering. Volume 3: Materials Technology; Ocean Space Utilization. Nantes, France*, V003T05A027. 10.1016/j.oceaneng.2021.10984610.1115/OMAE2013-11446.

Faltinsen, O.M. and Shen, Y. (2018). Wave and Current Effects on Floating Fish Farms. *J. Mar. Sci. Appl.*, **17**, 284–296. 10.1016/j.oceaneng.2021.10984610.1007/s11804-018-0033-5.

García, S., Trueba, A., Boullosa-Falces, D., Islam, H. and Guedes Soares, C. (2020). Predicting ship frictional resistance due to biofouling using Reynolds-averaged Navier-Stokes simulations. *Appl. Ocean Res.*, **62**, 100–118. 10.1016/j.oceaneng.2021.10984610.1016/j.apor.2020.102203.

Geremia, P. and de Villiers, E. (2012). A Comprehensive Tour of snappyHexMesh with HELYX-OS. Technical Report November, Engys.

Germano, M., Piomelli, U., Moin, P. and Cabot, W.H. (1991). A dynamic subgrid-scale eddy viscosity model. *Phys. Fluids A Fluid Dyn.*, **3**(7), 1760–1765. ISSN 0899-8213. 10.1016/j.oceaneng.2021.10984610.1063/1.857955.

Harendza, A., Visscher, J., Gansel, L. and Pettersen, B. (2008). PIV on inclined cylinder shaped fish cages in a current and the resulting flow field. In: *Proceedings of the International Conference on Offshore Mechanics and Arctic Engineering. Volume 4: Ocean Engineering; Offshore Renewable Energy. Estoril, Portugal. June 15–20*, 555–563. 10.1016/j.oceaneng.2021.10984610.1115/OMAE2008-57748.

Henderson, R.D. (1997). Nonlinear dynamics and pattern formation in turbulent wake transition. *J. Fluid Mech.*, **352**, 65–112. 10.1016/j.oceaneng.2021.10984610.1017/S0022112097007465.

Jung, J.H. and Yoon, H.S. (2014). Large eddy simulation of flow over a twisted cylinder at a subcritical Reynolds number. *J. Fluid Mech.*, **759**, 579–611. 10.1016/j.oceaneng.2021.10984610.1017/jfm.2014.581.

Katopodes, N.D. (2019). Chapter 8 - Turbulent Flow. In: N.D.B.T.F.S.F. Katopodes (Editor), *Free. Flow*, 566–650. Butterworth-Heinemann. ISBN 978-0-12-815489-2. 10.1016/j.oceaneng.2021.109846https://doi.org/10.1016/B978-0-12-815489-2.00008-3.

Klebert, P., Lader, P., Gansel, L. and Oppedal, F. (2013). Hydrodynamic interactions on net panel and aquaculture fish cages: A review. *Ocean Eng.*, **58**, 260–274. 10.1016/j.oceaneng.2021.10984610.1016/j.oceaneng.2012.11.006.

Klebert, P. and Su, B. (2020). Turbulence and flow field alterations inside a fish sea cage and its wake. *Appl. Ocean Res.*, **98**, 102113. 10.1016/j.oceaneng.2021.10984610.1016/j.apor.2020.102113.

Koide, M., Takahashi, T., Shirakashi, M. and Salim, S.A.Z.B.S. (2017). Three-dimensional structure of longitudinal vortices shedding from cruciform two-cylinder systems with different geometries. *J. Vis. (Tokyo)*, **20**, 753–763. 10.1016/j.oceaneng.2021.10984610.1007/s12650-017-0419-5.

Kristiansen, T. and Faltinsen, O.M. (2012). Modelling of current loads on aquaculture net cages. *J. Fluids Struct.*, **34**, 218–235. 10.1016/j.oceaneng.2021.10984610.1016/j.jfluidstructs.2012.04.001.

Lader, P., Enerhaug, B., Fredheim, A., Klebert, P. and Pettersen, B. (2014). Forces on a cruciform/sphere structure in uniform current. *Ocean Eng.*, **82**, 180–190. 10.1016/j.oceaneng.2021.10984610.1016/j.oceaneng.2014.03.007.

Lei, C., Cheng, L. and Kavanagh, K. (2001). Spanwise length effects on three-dimensional modelling of flow over a circular cylinder. *Comput. Methods Appl. Mech. Eng.*, **190**(22), 2909–2923. 10.1016/j.oceaneng.2021.10984610.1016/S0045-7825(00)00272-3.

Lilly, D.K. (1992). A proposed modification of the Germano subgrid-scale closure method. *Phys. Fluids A Fluid Dyn.*, **4**(3), 633–635. 10.1016/j.oceaneng.2021.10984610.1063/1.858280.

Løland, G. (1991). *Current Forces on and Flow through Fish Farms*. Ph.D. thesis, NTNU, Trondheim, Norway.

Lourenco, L.M. (1994). Characteristics of the plate turbulent near wake of a circular cylinder. a particle image velocimetry study. *published in Beaudan and Moin Beaudan and Moin (1994)*.

Ma, X., Karamanos, G.S. and Karniadakis, G.E. (2000). Dynamics and low-dimensionality of a turbulent near wake. *J. Fluid Mech.*, **410**, 29–65. 10.1016/j.oceaneng.2021.10984610.1017/S0022112099007934.

Norberg, C. (1994). An experimental investigation of the flow around a circular cylinder: Influence of aspect ratio. *J. Fluid Mech.*, **258**, 287–316. 10.1016/j.oceaneng.2021.10984610.1017/S0022112094003332.

Norberg, C. (2002). Pressure Distributions around a Circular Cylinder in Cross-Flow. In: *Symposium on Bluff Body Wakes and Vortex-Induced Vibrations (BBVIV3)At: Port Arthur, Queensland, Australia*, 1–4.

Osaka, H., Nakamura, I., Yamada, H., Kuwata, Y. and Kageyama, Y. (1983*a*). The structure of a turbulent wake behind a cruciform circular cylinder : 1st report, the mean velocity field. *Bull. JSME*, **26**(213), 356–363. 10.1016/j.oceaneng.2021.10984610.1299/jsme1958.26.356.

Osaka, H., Yamada, H., Nakamura, I., Kuwata, Y. and Kageyama, Y. (1983*b*). The structure of a turbulent wake behind a cruciform circular cylinder : 2nd report, the streamwise development of turbulent flow field. *Bull. JSME*, **26**(214), 521–528. 10.1016/j.oceaneng.2021.10984610.1299/jsme1958.26.521.

Parnaudeau, P., Carlier, J., Heitz, D. and Lamballais, E. (2008). Experimental and numerical studies of the flow over a circular cylinder at reynolds number 3900. *Phys. Fluids*, **20**(8), 085101. 10.1016/j.oceaneng.2021.10984610.1063/1.2957018.

Pope, S.B. (2000). *Turbulent Flows*. Cambridge University Press, Cambridge. ISBN 9780521598866. 10.1016/j.oceaneng.2021.109846DOI: 10.1017/CBO9780511840531.

Puzdrowska, M. and Heese, T. (2019). Detailed research on the turbulent kinetic energy's distribution in fishways in reference to the bolt fishway. *Fluids*, **4**(2), 64. 10.1016/j.oceaneng.2021.10984610.3390/fluids4020064.

Scarano, F. and Poelma, C. (2009). Three-dimensional vorticity patterns of cylinder wakes. *Exp Fluids*, **47**, 69–83. 10.1016/j.oceaneng.2021.10984610.1007/s00348-009-0629-2.

Smagorinsky, J. (1963). General circulation experiments with the primitive equations: I. The basic experiment. *Mon. Weather Rev.*, **91**(3), 99–164. 10.1016/j.oceaneng.2021.10984610.1175/1520-0493(1963)091¡0099:GCEWTP¿2.3.CO;2.

Sun, M. (2009). *The material and technology of fishing gear (in Chinese)*. China Agricultural Press. ISBN 9787109135888.

Tang, H., Hu, F., Xu, L., Dong, S., Zhou, C. and Wang, X. (2017). The effect of netting solidity ratio and inclined angle on the hydrodynamic characteristics of knotless polyethylene netting. *J. Ocean Univ. China*, **16**(5), 814–822. 10.1016/j.oceaneng.2021.10984610.1007/s11802-017-3227-6.

Tang, H., Hu, F., Xu, L., Dong, S., Zhou, C. and Wang, X. (2019). Variations in hydrodynamic characteristics of netting panels with various twine materials, knot types, and weave patterns at small attack angles. *Sci. Rep.*, **9**(1), 1923. 10.1016/j.oceaneng.2021.10984610.1038/s41598-018-35907-1.

Tang, M.F., Dong, G.H., Xu, T.J., Bi, C.w. and Wang, S. (2021). Large-eddy simulations of flow past cruciform circular cylinders in subcritical Reynolds numbers. *Ocean Eng.*, **220**, 108484. 10.1016/j.oceaneng.2021.10984610.1016/j.oceaneng.2020.108484.

Tsukrov, I., Drach, A., DeCew, J., Swift, M.R. and Celikkol, B. (2011). Characterization of geometry and normal drag coefficients of copper nets. *Ocean Eng.*, **38**(17), 1979–1988. 10.1016/j.oceaneng.2021.10984610.1016/j.oceaneng.2011.09.019.

Tu, G., Liu, H., Ru, Z., Shao, D., Yang, W., Sun, T., Wang, H. and Gao, Y. (2020). Numerical analysis of the flows around fishing plane nets using the lattice Boltzmann method. *Ocean Eng.*, **214**, 107623. 10.1016/j.oceaneng.2021.10984610.1016/j.oceaneng.2020.107623.

Vassiliadis, S.G. and Provatidis, C.G. (2004). Structural characterization of textile fabrics using surface roughness data. *Int. J. Cloth. Sci. Technol.*, **16**(5), 445–457. 10.1016/j.oceaneng.2021.10984610.1108/09556220410554633.

Wang, G., Martin, T., Huang, L. and Bihs, H. (2021). Modeling the flow around and the hydrodynamic drag on net meshes using REEF3D. *J. Offshore Mech. Arct. Eng.*, 1–21. ISSN 0892-7219. 10.1016/j.oceaneng.2021.10984610.1115/1.4051408.

Wang, X., Huang, L., Tang, Y., Zhao, F. and Sun, P. (2019). Two-dimensional numerical simulation of vortex shedding of multiple stranded ropes. In: *Proceedings of the International Conference on Offshore Mechanics and Arctic Engineering - OMAE*, V009T13A004. 10.1016/j.oceaneng.2021.10984610.1115/OMAE2019-95225.

Warming, R.F. and Beam, R.M. (1976). Upwind second-order difference schemes and applications in aerodynamic flows. *AIAA J.*, **14**(9), 1241–1249. 10.1016/j.oceaneng.2021.10984610.2514/3.61457.

Yue, P., Zhang, Q., Wang, R., Li, Y. and Wang, S. (2015). Turbulence intensity and turbulent kinetic energy parameters over a heterogeneous terrain of Loess Plateau. *Adv Atmos Sci*, **32**(9), 1291–1302. 10.1016/j.oceaneng.2021.10984610.1007/s00376-015-4258-9.

Zhao, M., Cheng, L. and Zhou, T. (2009). Direct numerical simulation of three-dimensional flow past a yawed circular cylinder of infinite length. *J. Fluids Struct.*, **25**(5), 831–847. 10.1016/j.oceaneng.2021.10984610.1016/j.jfluidstructs.2009.02.004.

Zhao, M. and Lu, L. (2018). Numerical simulation of flow past two circular cylinders in cruciform arrangement. *J. Fluid Mech.*, **848**, 1013–1039. 10.1016/j.oceaneng.2021.10984610.1017/jfm.2018.380.

Zheng, Z.Q., Wan, R., Chang, Z.Y., Zhang, Y. and Tao, J. (2019). Analysis of plane netting with twine breakage in aquaculture net cage. *J. Mar. Sci. Technol.*, **27**(1), 72–76. 10.1016/j.oceaneng.2021.10984610.6119/JMST.201902_27(1).0009.

Zhou, C., Xu, L., Hu, F. and Qu, X. (2015). Hydrodynamic characteristics of knotless nylon netting normal to free stream and effect of inclination. *Ocean Eng.*, **110**, 89–97. 10.1016/j.oceaneng.2021.10984610.1016/j.oceaneng.2015.09.043.

Zhou, J., Adrian, R.J., Balachandar, S. and Kendall, T.M. (1999). Mechanisms for generating coherent packets of hairpin vortices in channel flow. *J. Fluid Mech.*, **387**, 353–396. 10.1016/j.oceaneng.2021.10984610.1017/S002211209900467X.